UNIVERSITÀ DEGLI STUDI DI FIRENZE
DIPARTIMENTO DI FISICA E ASTRONOMIA

Scuola di Dottorato in Scienze
DOTTORATO DI RICERCA IN FISICA - XXIII CICLO
SSD FIS/03 Fisica della Materia

Dissertation in Physics

TO OBTAIN THE DEGREE OF

Dottore di Ricerca
in Fisica

TITLE:

Optical Multi-Dimensional Analysis of Human Tissues

PRESENTED BY

Alessandro Cosci

Supervisor   PROF. FRANCESCO S. PAVONE

Coordinator   PROF. ALESSANDRO CUCCOLI

December 2010

Contents

CONTENTS

Chapter 1

Introduction

The aim of this thesis is the optical investigation of human tissues. Diagnosis of human diseases using light started in the middle of the 19th century, even if the optical investigation in biology was already a well-suited method performed by using the microscope developed in the previous centuries. Biological tissues can be considered opaque media in which light can be absorbed, reflected or scattered. Light penetration in tissues depends on their water content and on the absorption of molecular components, which can exhibit a particular spectrum. High absorption by water occurs in both ultraviolet (UV) and infrared (IR, $\lambda > 2\mu$m) spectral range. In the visible light range (300 nm - 700 nm) both scattering and absorption can occur. The latter is due to the absorption of the endogenous molecules. In the range of 700 nm - 1500 nm scattering dominates and light can penetrate deeper into the tissue. Therefore this range is called *optical therapeutic window of tissues*. The emission of Ti:Sapphire pulsed lasers is in the range of 700 nm - 1000 nm, hence it is well-suited for deep tissue investigation. By means of femtosecond pulses it is possible to use non-linear spectroscopy, as two-photon excitation and second-harmonic generation, in order to explore optical processes with transition energies in the range of visible light. In this thesis I have investigated human skin and bladder mucosa by means of two-photon endogenous fluorescence and second-harmonic generation microscopy. Using a custom-built two-photon microscope, equipped with a photon counting unit

for time-resolved fluorescence spectroscopy, both morphological and spectroscopic investigation of biological tissues can be performed. Two studies will be presented, one on human bladder carcinoma *in situ* and the other on dermatological disorder of human dermis. I have highlighted the capabilities of non-linear microscopy in providing an extensive tissue characterization by means of its spectroscopic and morphological features.

In this work I have also presented and characterized a custom-built optical fiber-probe for *in vivo* mesurements. The probe was designed in order to perform fluorescence spectrocopy and lifetime measurements, with the main concept of fast acquisition time and high flexibility. Furthermore, due to its small size (outer diameter 2.1mm), it is meant to be used in a service channel of commercial cystoscope.

This thesis is organized in three main parts:

- In the first part, Chapter 2, the theoretical background is introduced. The two main phenomena used in two-photon microscopy, as two photon excitation and second-harmonic generation, are described. It will be highlighted their dependence on the square of the intensity (I^2) and their consequences on the microscope capabilities. Afterwards, the two main techniques for fluorescence lifetime measurements (time domain and frequency domain) will be described.

- In the second part, Chapter 3, I am going to present and characterize the set-ups used in this thesis work: a custom-built two-photon microscope and an optical fiber-probe. The former will be characterized in terms of spatial and temporal resolution. The latter will be described, calibrated and tested on human skin.

- In the third part, Chapter 4 and 5, I am going to present two studies on human bladder and skin. A characterization of bladder carcinoma *in situ*, its spectroscopic and morphological features will be shown in comparison with a similar analysis performed in healthy mucosa. In chapter 5 I am going to use three different image pattern analysis methods in

order to characterize the organization of collagen fibers in healthy dermis, normal scars and keloids.

1.1 Human tissue anatomy: skin and bladder

Biological tissues are composed by two main layers: one superficial cellular layer, called epithelium, and another deeper layer, composed of collagen and elastic fiber, called connective tissue. In this work I examined tissue samples of both human skin and bladder. The anatomy of these two biological tissues is described in detail in the following paragraphs.
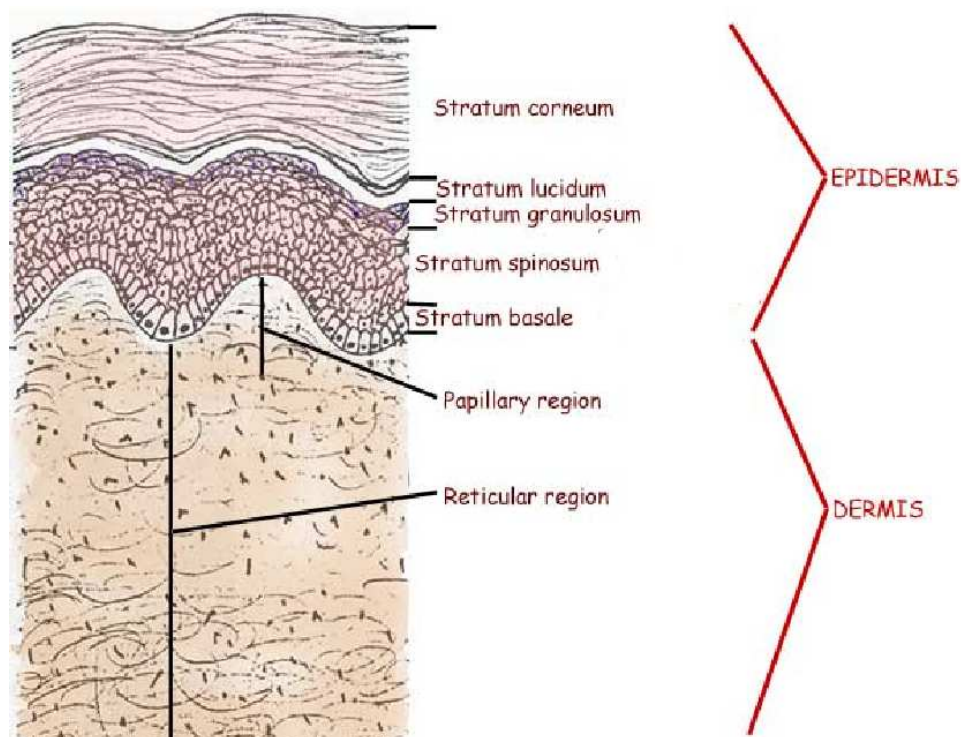
1.1.1 Human skin

Figure 1.1: Layers in skin epidermis and dermis

Skin epithelium is also referred as epidermis and it is conventionally divided in 5 layers characterized by peculiar architecture and protein expression. These layers are, from the deeper to the upper:

- *Stratum Basale*: it is composed by a single cellular layer. Cells are cylindrical or cubical, showing high proliferation and they are attached to the basal membrane by hemidesmosomes. Cells containing melanin, melanocytes, are located mainly in this layer.

- *Stratum Spinosum*: it is a multi-layer of poliedric cells, which are becoming more flattened getting closer to the surface. Cells show radially oriented cytoplasmic extension yielding to a "spinosum" aspect. *Stratum Spinosum* exhibits high lipid content for preventing skin dehydratation.

- *Stratum Granulosum*: it is composed by a layer of oblong and flattened cells showing small nuclei.

- *Stratum Lucidum*: it is a layer of flattened cells which appear translucent under the microscope. Cells are dead and most of them exhibit a lack of nucleus.

- *Stratum Corneum*: It is a multi-layer of dead flattened cells. Its thickness depends on the body location. Cells exhibit a completely lack of nucleus, a thick membrane and they are containing keratin in high concentration. It separates the living tissue from the external environment.

Skin connective tissue is commonly called dermis. It is characterized by a lower cellular content and its main components are elastic and collagen fibers. The former are arranged in a reticular pattern and they are responsible of skin elasticity; the latter are arranged in fiber bundles and they are responsible of skin strength. Both elastin and collagen are produced by special cells called fibroblasts. Dermis is also sub-divided in two different parts: *Stratum Papillare* and *Stratum Reticulare*. The former shows thin collagen

fibers arranged perpendicular to the epidermis, with which they are in contact, forming crests called *papillae*. This region is reached by capillary blood vessels and nervous endings. In the *Stratum Reticulare* collagen fibers are thicker and arranged parallel to the epidermal surface.

1.1.2   Human bladder urothelium

Human bladder transitional epithelium, also known as urothelium, has a different conformation with respect to epidermis because this tissue should allow stretching and relaxing of the bladder. Transitional epithelium is a multi-layer of cells that exhibit the capability to contract and to expand in order to be versatile for tissue dilatation. In the relaxed position cells are cubical, while their shape becomes squamous with bladder dilatation (Fig.1.2).

The urothelium has a typical thickness of about 50 μm. In the deeper layers of bladder tissue I find a connective tissue, mainly composed by elastin and collagen, showing similarities in comparison with skin dermis.
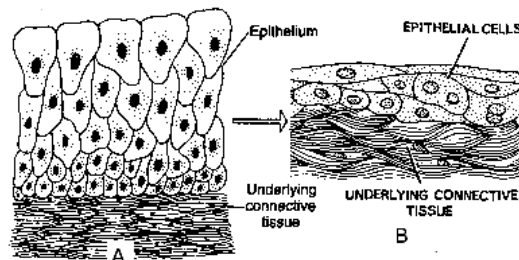

Figure 1.2: Cell morphology of transitional epithelium for relaxed (A) and stretched (B) urinary bladder [1].

1.2   Microscopy

The origin of the microscope is credited to two Dutch spectacle-makers in 1597, Hans and Zacharias Jenssen. By inserting two lenses in a tube they

were able to magnify small objects. Their invention was a forerunner both for the microscope and for the telescope. Later Anthony Van Leeuwenhoek (1632-1723), the father of microscopy, perfected the methods for producing lenses, improving grinding and polish procedures. He could realize a high magnification microscope with which he observed for the first time bacteria, yeast plants and circulation of blood corpuscles in capillary. In 1665 Robert Hooke published *Micrographia*, a milestone for microscopy, which included the discovery of plant cells. Using double convex or spherical lenses with short focal length he was able to improve the magnification.

In the 18th-19th centuries the main improvements of the microscope were in mechanics. The new microscopes had more stability and the possibility to tune focus and magnification. Moreover the development of objective lenses introduced improvements on both resolution and magnification. In 1880 Zeiss produced the first oil immersion microscope, designed by Ernst Abbe, the founder of optical theory of microscope lenses.

Further progresses arose in the 20th century. In 1934 Zernike developed the phase contrast microscope, in 1953 Normansky patented the differential interference microscope, in 1975 modulation contrast microscopy was discovered by Hoffman and Gross [2].

Fluorescence microscopy was developed almost 100 years ago. Using UV light it was possible to achieve higher resolution. At the beginning the studies were restricted to only natural fluorescent specimens, but almost immediately new investigations started on fluorescent dyes for tissue staining. In 1950 a breakthrough in microscopy was introduced by Coons and Kaplan which developed a technique for labeling antibodies with a fluorescent dye, giving rise to immunohistochemistry [3].

In 1994 the Nobel prize Chalfie [4] genetically encoded a fluorescent protein (GFP), naturally found in the jellyfish *aequorea victoria*, in *Escherichia coli* bacteria, starting a new era for microscopy. The combination of fluorescence microscopy with genetically fluorescent organism opened a new frontier in modern biology.

A further improvement in both axial and radial resolution arose from confocal imaging. Widefield microscopy is limited in resolution to 2 μm, since the

light from the "out-of-focus" regions are interfering with the signal from the region of interest. Confocal imaging uses a spatial filter (pinhole) in order to get rid of the out of focus signal. It usually employs laser scanning and the images produced are called "optical sections". The principle of confocal microscopy was developed by Marvin Minsky in 1950s, but the first laser scanning confocal microscope was realized by Brakenhoff [5] only in the 1979. Almost simultaneously Sheppard contributed with the theory of image formation [6]. New improvements came from the end of the 20th century with the diffusion of non-linear microscopy. This new imaging techniques provides several advantages with respect to traditional fluorescence techniques as described in the next paragraph.

1.2.1   Two-photon microscopy

A new powerful microscopy method was established in 1990 by Denk, Strickler and Webb [7]: the two-photon laser scanning fluorescence microscope. This technique uses the phenomenon of two-photon absorption in order to excite the sample only at the focal point. Since the transition probability is proportional to the squared intensity of the laser beam, there is no need of a spatial filter. Tissue exposure and photobleaching are strongly reduced with respect to equivalent confocal microscopy. Furthermore, due to the fact that it uses IR light, it is possible to image deeper inside biological tissues. The two-photon excitation was predicted by Maria Göppert-Mayer [8] more than 70 years ago, but only with the rise of high power femtosecond-pulsed lasers it was possible to employ this phenomenon in microscopy.

Since its invention, the two-photon microscope has been involved in many research fields of life science [9, 10]. Two-photon excited fluorescence (TPEF) microscopy found applications in the study of biological mechanisms inside cells [11] as well as in the investigation and spectroscopy of fluorescence proteins [12, 13, 14]. New technological achievements in this last decade made possible TPEF microscopy *in vivo* on animal [15] and human model [16]. Two-photon microscope for *in vivo* human skin analysis is already com-

mercially available [17, 18]. Using new fiber optic technologies [19] TPEF microscopy could be also applied to endoscopy [20, 21, 22].

Beside TPEF, second-harmonic generation (SHG) microscopy is a powerful tool of immediate implementation in a two-photon microscope. SHG is a non-linear second-order scattering phenomenon. It occurs in molecules without center of symmetry and high hyperpolarizability. Through SHG non-centrosymmetric molecules inside cells [23], cell membranes[24], brain [25] and biological tissues [26] have been investigated. SHG microscopy is a well-suited technique for imaging collagen, a protein typical of connective tissues exhibiting fibrillar structure and high hyperpolarizability. The potential of this technique in collagen investigation has been demonstrated by studies on structural changes in fibrotic collagen [27], human dermis [28, 29], keloids [30], cornea [31, 32] and tumor microenvironment [33].

An additional improvement is represented by multi-spectral TPEF (MTPE) in which, by using a spectrograph and a multi-channel PMT array as detector, it is possible to combine TPEF microscopy with fluorescence spectroscopy. As result, instead of having a grey-scale image in which the intensity corresponds to the whole emitted fluorescence, it can be obtained a set of images, one per fluorescence channel.

A further enhancement in tissue investigation by two-photon microscope arises from the analysis of fluorescence dynamics. By determination of fluorescence lifetime of a molecule it is possible to extract information about its molecular microenvironment. Fluorescence lifetime imaging microscopy (FLIM) is a technique that combines microscopy and lifetime measurements, in which for each acquired pixel a fluorescence decay profile is recorded. Therefore the image, beside providing information on the emitted fluorescence intensity, contains information on the fluorescence dynamics pixel by pixel. FLIM was already demonstrated to be a powerful tool for investigating molecular microenvironment [34], protein localization [35] and protein-protein interaction [36, 37].

1.3 Optical multi-dimensional analysis of human tissues

This thesis focuses on the "optical multidimensional analysis of human tissues", by using a custom-built two-photon microscope, equipped with FLIM and MTPE capabilities. The experimental set-up allows studies on a multidimensional space. In fact, together with the spatial coordinates, temporal and spectral coordinates are examined so that the samples are characterized in a five-dimensional space (x, y, z, t, λ). By imaging the tissue it is possible to investigate its morphology. By investigating the fluorescence lifetime with FLIM, it is possible to add another "dimension" corresponding to the fluorescence lifetime. A further "dimension" is coming from the multi-spectral TPEF. Finally, by combining all these techniques, we can obtain for each acquisition on the sample a 3-D image of its morphology (TPEF and SHG) and, for each pixel of the image, a corresponding fluorescence spectrum and a corresponding fluorescence decay profile. Therefore it is called multi-dimensional analysis.

In vivo optical multi-dimensional analysis can be also reffered as "optical biopsy". In fact, as conventional biopsies, this technique is capable to give information about the morphology of the tissue and also, by means of fluorescence spectroscopy and lifetime measurements, about its molecular composition and metabolism. With respect to conventional biopsies, optical biopsies have the main advantage to be less invasive. Moreover, it can give an immediate response, saving both time and money in comparison with traditional diagnostic techniques.

Since in multi-dimensional analysis a huge amount of data is collected, we need to assign for each acquired data-set one or more score indices in order to achieve a fast response. A score is a result of a calculation on the acquired information, usually expressed numerically, that enhances the differences between two or more data-sets acquired from different physiologically samples. For example, in this thesis I highlighted the balance between nicotinamide adenine dinucleotide (NADH) and flavin adenine dinucleotide (FAD) by using

the Red-Ox ratio defined as follows:

$$RedOx = \frac{FAD - NADH}{NADH + FAD} \tag{1.1}$$

I considered their concentration to be proportional to the fluorescence signal acquired in two different spectral regions and excited using two different wavelengths. This score is normalized so that it varies between -1 and 1. A value of the score close to -1 is evidencing a predominance of NADH inside cells.

Morphological scores are really important in tissue characterization and discrimination. An image acquired using a two-photon microscope has a huge amount of information and it is really complex to analyze. Scores arising from pattern analysis or from cellular to nuclear dimension ratio [38] can highlight important feautures of the tissue as collagen organization inside dermis or cellular proliferation in cancer. These methods are meant to be a powerful tool in morphological staging performed by pathologists. Moreover, such a method can provide a classification indipendent from human subjectivity.

As asserted above, tissue diseases have their own "fingerprint" in terms of morphology and molecular composition. A morphological "fingerprint" of cancer can be the ratio between cellular to nuclear dimension ratio [38]. Moreover histology, the golden standard for tissue diagnosis, is mainly based on a morphological characterization of the tissue after staining.

Chemical "fingerprint" of a disease could be measured through MTPE. In case of cancer fluorescence spectroscopy can yield to important information on the cellular metabolism. In fact, according to the Warburg effect [39] (a complete description this effect will be given in paragraph 4.2), in tumoral cells ATP production is preferably due to glycolysis, while in healthy cells phosphorylation dominates. Nicotinamide adenine dinucleotide (NADH) molecule is involved in both glycolysis and phosphorylation, but in the latter another molecule such as flavin adenine dinucleotide (FAD) is also involved. These two molecules show different absorption and emission spectra. Therefore by evaluating the balance between this two molecules, it is possible to have an indicator about cellular metabolism [40].

Chemical "fingerprint" of cellular metabolism can be also measured by means of FLIM, since FAD and NADH fluorescence lifetimes varie of about one order of magnitude depending if they are free or in a protein-bound state. Therefore, by measuring their fluorescence lifetime, it is possible to understand if they are free or protein-bound, and hence to have further characterization of the tissue under investigation.

1.3.1 Multi-dimensional fiber-probe

My PhD project involved also the designing and the realization of a multi-dimensional fiber-probe for *in vivo* measurements, which require fast acquisition time, therefore a short time exposure for the patient, and high flexibility. The fiber-probe has a total outer diameter of 2.1 mm and hence it is possible to use it in a service channel of a commercial cystoscope. In order to have a fast acquisition time I decided to sacrifice the imaging capability, focusing on the tissue spectroscopic "fingerprint" by means of fluorescence spectroscopy and lifetime. The information coming out from the probe arises from a small excited volume of the tissue without providing any image.

1.3.2 Conclusion

During my PhD I used multi-dimensional analysis on two different diseases as bladder carcinoma *in situ* (CIS) and keloid. The former study consisted mainly in tissue characterization through fluorescence spectroscopy and lifetime, whilst in the latter I characterized collagen pattern of keloids mainly by morphological investigation. In this way I show two different features of multi-dimensional analysis through two-photon microscopy, morphological and spectroscopic.The main purpose of this work is to find the right score indices, in the multi-dimensional acquired data-sets, in order to highlight the differences, in both morphology and spectroscopy, between healthy and pathologic tissues.

As result of my studies I show all the potential of the combination of morphology with spectroscopy. Finally I can claim that optical multi-dimensional

analysis has the potential to be a powerful tool for diagnosis, investigation and pharmaceutical follow-up of human diseases.

Chapter 2

Theoretical background

This chapter describes the theoretical background of the thesis. We start introducing the light matter interaction, especially single and two-photon absorption and second-harmonic generation. The non-linear dependence from the light intensity of the last two phenomena gives rise to important features in the two-photon microscope. Finally we describe the main techniques for fluorescence lifetime measurement and imaging.

2.1 Two-photon microscopy

In this section the basic theory of two-photon microscopy is presented. We will show that different phenomena as two-photon absorption and second-harmonic generation have the same dependence on the square of the intensity (I^2). Then, we present the consequences of this property on the spatial resolution of the microscope.

2.1.1 Single- and two-photon absorption

Single-photon absorption

In this paragraph we describe the interaction of light with an atomic system. For semplicity we use the semi-classical picture in which light is treated as a periodic perturbation acting on an atomic system.

Let's call H_o the Hamiltonian of the unperturbed atom and $\lambda V(t)$ the perturbation due to the incident electromagnetic field

$$H(t) = H_o + \lambda V(t). \tag{2.1}$$

In absence of perturbation the energy levels of the atom are the eigenvalues of H_o

$$H_o|n> = \epsilon_n|n> \tag{2.2}$$

By applying the temporal propagator to the eigenstate we find a phase factor describing the temporal evolution

$$|n(t)> = e^{-i\frac{\epsilon_n}{\hbar}t}|n> = e^{-i\omega_n t}|n> . \tag{2.3}$$

In presence of perturbation, the generic eigenstate of the perturbed Hamiltonian $H(t) = H_o + \lambda V(t)$ can be written as linear combination of the eigenstates of H_o

$$|\phi(t)> = \sum_n c_n(t)e^{-i\omega_n t}|n> . \tag{2.4}$$

We can then expand the coeffiecients $c_n(t)$ in powers of λ

$$c_n(t) = c_n^{(o)}(t) + \lambda c_n^{(1)}(t) + \lambda^2 c_n^{(2)}(t) + ... \tag{2.5}$$

Using the Schroedinger equation

$$i\hbar \frac{\partial}{\partial t}|\phi(t)> = H(t)|\phi(t)> \tag{2.6}$$

projecting on $<k|$ and considering coefficients with the same power of λ, we obtain

$$\frac{\partial}{\partial t}c_k^{(s+1)}(t) = -\frac{i}{\hbar}\sum_n c_n^{(s)}V_{kn}(t)e^{-i(\omega_n-\omega_k)t} \tag{2.7}$$

where $V_{kn} = <k|V(t)|n>$ and $\frac{\partial}{\partial t}c_n^{(0)}(t) = 0$.

Then it is possible to add, by phenomenological consideration, a relaxation

term

$$\frac{\partial}{\partial t}c_k^{(s+1)}(t) = -\frac{i}{\hbar}\sum_n c_n^{(s)}V_{kn}(t)e^{-i(\omega_n-\omega_k)t} - \frac{\gamma_k}{2}c_k^{(s+1)}(t). \qquad (2.8)$$

We can assume that at time $t = 0$ the perturbation is not present and the system occupies the eigenstate $|m>$ of the unperturbed hamiltonian

$$c_k^{(0)}(t) = \delta_{km} \qquad (2.9)$$

Then by inserting $c_k^{(0)}(t)$ in the expression for $c_k^{(1)}(t)$ we obtain

$$\frac{\partial}{\partial t}c_k^{(1)}(t) = -\frac{i}{\hbar}e^{-i(\omega_m-\omega_k)t}V_{km}(t) - \frac{\gamma_k}{2}c_k^{(1)}(t). \qquad (2.10)$$

In the dipole approximation the light interaction term $V_{km}(t)$ can be written as

$$V_{km}(t) = -\frac{E\mu_{km}}{2}e^{-i\omega t} + \frac{E\mu_{km}}{2}e^{i\omega t}. \qquad (2.11)$$

Substituting it in eq.(2.10) yields

$$c_k^{(1)}(t) = -\frac{iE\mu_{km}}{2\hbar}\frac{e^{i(\omega_{km}-\omega)t} - e^{\frac{\gamma_k}{2}t}}{i(\omega_{km}-\omega) + \frac{\gamma_k}{2}t} + \frac{iE\mu_{km}}{2\hbar}\frac{e^{i(\omega_{km}+\omega)t} - e^{\frac{\gamma_k}{2}t}}{i(\omega_{km}+\omega) + \frac{\gamma_k}{2}t} \qquad (2.12)$$

where $\omega_{km} = \omega_k - \omega_m$.

In proximity of the resonance frequency, $\omega \sim \omega_{km}$, it is possible to neglect the second term of the equation (Rotating Wave Approximation), obtaining

$$c_k^{(1)}(t) = -\frac{iE\mu_{km}}{2\hbar}\frac{e^{i(\omega_{km}-\omega)t} - e^{\frac{\gamma_k}{2}t}}{i(\omega_{km}-\omega) + \frac{\gamma_k}{2}t}. \qquad (2.13)$$

The probability to find the system in the state $|k>$ at time t, it is just the square module of $c_k^{(1)}(t)$

$$|c_k^{(1)}(t)|^2 = \frac{E^2\mu_{km}^2}{4\hbar^2}\frac{\sin^2\left[\frac{(\omega_{km}-\omega)t}{2}\right]}{\left[\frac{(\omega_{km}-\omega)}{2}\right]^2}exp(-\gamma_k t). \qquad (2.14)$$

We can finally point out that the transition probability from the state $|m>$ to the state $|k>$ due to one photon absorption is proportional to E^2,

hence to the light intensity, and it has a resonance for $\omega = \omega_{km}$.

Two-photon absorption

The possibility that an electronic transition occurs by simultaneus absorption of two or more photons was predicted in 1931 by Maria Göppert-Mayer[8], but the first experimental observation was made only 30 years later by Kaiser and Garret[41] who measured a two-photon transition in a crystal of $CaF_2 : Eu^{2+}$. In two-photon excitation the transition probability is calculated from $c_k^{(2)}(t)$ using the second order perturbation theory.

$$\frac{\partial}{\partial t}c_k^{(2)}(t) = -\frac{i}{\hbar}\sum_i c_i^{(1)}V_{ki}(t)e^{-i(\omega_i - \omega_k)t} - \frac{\gamma_k}{2}c_k^{(2)}(t). \qquad (2.15)$$

By the insertion of $c_i^{(1)}$ and $V_{ki}(t)$

$$\frac{\partial}{\partial t}c_k^{(2)}(t) = -i\left(\frac{E}{2\hbar}\right)^2 \sum_i \frac{\mu_{mi}\mu_{ik}}{(\omega_{mi} - \omega) + i\frac{\gamma_i}{2}}\left[e^{[i(\omega_{mk} - 2\omega)t]} - e^{[i(\omega_{im} - \omega)t - \frac{\gamma_i t}{2}]}\right]$$
$$- \frac{\gamma_k}{2}c_k^{(2)}(t).$$

$$(2.16)$$

In case of $2\omega \sim \omega_{km}$ the second exponential term has fast oscillations and it can be neglected in the integration yielding

$$c_k^{(2)}(t) = \left(\frac{E}{2\hbar}\right)^2 \sum_i \frac{\mu_{mi}\mu_{ik}}{(\omega_{mi} - \omega)}\frac{e^{[i(\omega_{mk} - 2\omega)t]} - e^{\frac{\gamma_k t}{2}}}{(\omega_{mk} - 2\omega) + i\frac{\gamma_k t}{2}} \qquad (2.17)$$

The transition probability is the square module of $c_k^{(2)}(t)$. Concerning the time dependence, in case of excitation time $\tau \ll \frac{1}{\gamma_k}$, it becomes:

$$|c_k^{(2)}|^2 \propto 4\frac{\sin^2[(\omega_{mk} - 2\omega)\frac{\tau}{2}]}{(\omega_{mk} - 2\omega)^2} \qquad (2.18)$$

evidencing a resonance for $2\omega \sim \omega_{mk}$. Regarding the amplitude

$$|c_k^{(2)}|^2 \propto E^4 = I^2. \qquad (2.19)$$

More in general, the total irradiated power by two photon excitation excited fluorescence (TPEF), could be written as:

$$P_{TPE} = \frac{1}{2}\sigma_{TPE}I_\omega^2 \tag{2.20}$$

where σ_{TPE} is the product between the two-photon fluorescence cross section and the fluorescence quantum yield. This property is one of the most important concerning the features of a two-photon microscope, involving the excitation volume and the microscope resolution, as it will be discussed later.

2.1.2 Second-Harmonic Generation

Another phenomena of non-linear optics is the generation of high order harmonics. In this paragraph we are concentrating on the second-harmonic generation (SHG). In linear optics the polarization $P(t)$ of a dielectric medium is proportional to electric field $E(t)$

$$P(t) = \chi^{(1)}E(t) \tag{2.21}$$

where $\chi^{(1)}$ is the linear susceptibility.
Besides, in non-linear optics the polarization is also proportional to higher order components of the electric field amplitude, negligible in case of linear polarization.

$$P(t) = \chi^{(1)}E(t) + \chi^{(2)}E(t)^2 + \chi^{(3)}E(t)^3 + ... =$$
$$= P^{(1)}(t) + P^{(2)}(t) + P^{(3)}(t) + ... \tag{2.22}$$

in case of oscillating electric field, $E(t) = E_0 exp(-i\omega t) + c.c.$, the second term originates the non-linear phenomenon known as second-harmonic generation (SHG) and its expression is

$$P^{(2)}(t) = 2\chi^{(2)}|E_0|^2 + (\chi^{(2)}|E_0|^2 exp(-2i\omega t) + c.c.) \tag{2.23}$$

the first term is a static field, while the second contains a term with an oscillation proportional to 2ω, responsible of SHG. In fact, the resulting oscillating

polarization is source for a new electric field following the Maxwell equation

$$\nabla^2 E - \frac{n^2}{c^2}\frac{\partial^2 E}{\partial t^2} = \frac{4\pi}{c^2}\frac{\partial^2 P}{\partial t^2} \tag{2.24}$$

The electric field generated by $P^{(2)}(t)$ is oscillating at frequency 2ω, with double frequency with respect to the fundamental one and therefore it is defined as second-harmonic.

Microscopic description

Inside a dielectric medium, in presence of an excitation electric field, every single molecule acts as a single dipole, $P(t)$ is the mean value of the dipole moment in a volume V

$$P(t) = \frac{1}{V}\int_V \mu(\vec{x})d\vec{x} \tag{2.25}$$

Let's suppose the oscillating electric field, with a frequency ω and amplitude E_ω, linearly polarized in $\hat{z}$. By using 2.22, the induced dipole moment at frequency 2ω has the following expression

$$\vec{\mu}_{2\omega} = \frac{1}{2}\chi_{zzz}E_\omega^2\hat{z} \tag{2.26}$$

where we considered only the component χ_{zzz} of the hyperpolarizability tensor. From 2.24 and 2.23 is possible then to calculate the second-harmonic far field at inclination ψ from the z axis

$$\vec{E}_{2\omega}(\psi) = -\frac{\mu_{2\omega}\omega^2}{\pi\varepsilon_0 c^2 r}\sin(\psi)exp(-i2\omega[t])\vec{\psi} \tag{2.27}$$

where c is the speed of light, ε_0 the free-space permittivity, r the observation distance from the dipole and $[t]$ the corresponding delay time. The corresponding irradiated power, expressed in $photon/second$, per differential solid angle at inclination angle ψ, can be written as

$$P_{2\omega}(\psi) = \frac{3}{16\pi}\sigma_{SHG}\sin^2(\psi)I_\omega^2 \tag{2.28}$$

where the intensity of the electric field I_ω is expressed in *photon/second* per unit area, and σ_{SHG} is the SHG cross section defined as

$$\sigma_{SHG} = \frac{4 n_{2\omega} \hbar \omega^5}{3\pi n_\omega^2 \varepsilon_0^3 c^5} |\chi_{zzz}|^2 \tag{2.29}$$

where n_ω and $n_{2\omega}$ are the medium refractive index at frequencies ω and 2ω, respectively. Integrating on the full solid angle it is possible to give a simple expression for the emitted SHG power

$$P_{SHG} = \frac{1}{2} \sigma_{SHG} I_\omega^2 \tag{2.30}$$

This expression could be easily compared with the eq.(2.20) that describes the power irradiated by two-photon excitation (TPEF)

$$P_{TPEF} = \frac{1}{2} \sigma_{TPE} I_\omega^2 \tag{2.31}$$

Since σ_{TPE} and σ_{SHG} could be expressed with the same units, these two last formulas are well suitable for direct comparison between the two phenomena.

Generalized SHG theory

Let's consider an oscillating electric field with a Gaussian profile propagating inside a medium, calling w_ρ and w_z the radial and axial beam waist, and ξ the effective reduction in the axial propagation vector caused by the Gouy shift

$$\vec{E}(\vec{x}) = -i E_\omega exp \left(-\frac{x^2 + y^2}{w_\rho^2} - \frac{z^2}{w_z^2} + i k_\omega \xi z \right) \hat{\epsilon} \tag{2.32}$$

Analyzing SHG, we can write the local second-harmonic dipole moment per unit scatterer concentration, using the relation

$$\vec{\mu}_{2\omega,i}(\vec{x}) = \frac{1}{2} E_\omega^2(\vec{x}) \sum_{j,k} \langle \chi_{ijk} \rangle \hat{e}_j \hat{e}_k \tag{2.33}$$

where $\langle \chi_{ijk} \rangle$ is the local ensemble-averaged hyperpolarizability unit density. Let's now change to spherical coordinates, defining the three unit vector as

$$
\begin{aligned}
\hat{r} &= \sin(\theta)\cos(\phi)\hat{x} + \sin(\theta)\sin(\phi)\hat{y} + \cos(\theta)\hat{z} & (2.34) \\
\hat{\theta} &= \cos(\theta)\cos(\phi)\hat{x} + \cos(\theta)\sin(\phi)\hat{y} - \sin(\theta)\hat{z} & (2.35) \\
\hat{\phi} &= -\sin(\phi)\hat{x} + \cos(\theta)\hat{y} & (2.36)
\end{aligned}
$$

If we consider just a single scattering element positioned in the focus and if we look, at an angle $\Theta = \{\theta, \phi\}$, the second-harmonic electric far-field generated is

$$
\vec{E}_{2\omega}^{(0)}(\Theta) = \begin{pmatrix} E_{2\omega}^{(0)p}(\Theta) \\ E_{2\omega}^{(0)s}(\Theta) \end{pmatrix} = \frac{\eta}{r} M \cdot \vec{\mu}_{2\omega}(0) \tag{2.37}
$$

where s and p are the two polarization components, $\eta = \omega^2/\pi\varepsilon_o c^2$ is the far field propagation distance $(rk_\omega \gg 1)$ to the observer and M is the projection matrix defined as

$$
M \begin{pmatrix} \hat{\theta} \\ \hat{\phi} \end{pmatrix} = \begin{pmatrix} \cos\theta\cos\phi & \cos\theta\sin\phi & -\sin\phi \\ -\sin\phi & \cos\phi & 0 \end{pmatrix} \tag{2.38}
$$

For simplicity we have assumed $n_\omega \sim n_{2\omega}$. In case of multiple scattering element, with a spatial distribution $N(\vec{x})$, we can write eq.(2.37) as follow

$$
\vec{E}_{2\omega}(\Theta) = \frac{\eta}{r} \int N(\vec{x}) M \cdot \vec{\mu}_{2\omega}(\vec{x}) exp(-ik_{2\omega}\vec{x} \cdot \hat{r}) d\vec{x} \tag{2.39}
$$

assuming $\langle \chi \rangle$ independent from the position. $N(\vec{x})$ can be expanded in Fourier components

$$
N(\vec{q}) = \left(\frac{k_{2\omega}}{2\pi} \right)^d \int N(\vec{x}) exp(-ik_{2\omega}\vec{q} \cdot \vec{x}) \tag{2.40}
$$

where d is the dimensionality of the scattering element distribution, and $\vec{q}$ represents a spatial wave vector. The total second-harmonic radiated field is the coherent summation of all the contribution from every single scattering

element

$$\vec{E}_{2\omega}(\Theta) = V_{(d)} \vec{E}_{2\omega}^{(0)}(\Theta) \int N(\vec{q}) A_{(d)}(\Omega, \vec{q}) d\vec{q} \tag{2.41}$$

where we also introduced a dependence from the dimensionality. $V_{(d)}$ is the active SHG volume and the phased summation of the radiated fields from the distributed sources gives rise to the antenna factor $A_{(d)}$. In order to investigate different geometry of the problem we can then introduce

$$A_x = exp\left(\frac{-k_{2\omega}^2 w_\rho^2 (\sin\theta\cos\phi - q_x)^2}{8}\right) \tag{2.42}$$

$$A_y = exp\left(\frac{-k_{2\omega}^2 w_\rho^2 (\sin\theta\cos\phi - q_y)^2}{8}\right) \tag{2.43}$$

$$A_z = exp\left(\frac{-k_{2\omega}^2 w_z^2 (\cos\theta - \xi - q_z)^2}{8}\right) \tag{2.44}$$

In case of the scattering element aligned and uniformly distributed on the z axis $(x, y = 0)$, we obtain:

$$V_{(1)} = \left(\frac{\pi}{2}\right)^{\frac{1}{2}} w_z \tag{2.45}$$

$$A_{(1)} = A_z \tag{2.46}$$

While in case they are distributed on a two-dimensional surface in the yz plane $(x=0)$, we obtain:

$$V_{(2)} = \left(\frac{\pi}{2}\right) w_\rho w_z \tag{2.47}$$

$$A_{(2)} = A_y A_z \tag{2.48}$$

and in case of a three dimensional distribution

$$V_{(3)} = \left(\frac{\pi}{2}\right)^{\frac{3}{2}} w_\rho^2 w_z \tag{2.49}$$

$$A_{(3)} = A_x A_y A_z \tag{2.50}$$

Finally we can write the SHG emitted power in the unit of solid angle in the direction Ω as

$$P_{2\omega}(\Omega) = \frac{1}{2} n\varepsilon_o cr^2 |\vec{E}_{2\omega}(\Theta)|^2 \tag{2.51}$$

2.1.3 Point spread function and spatial resolution

In the previous subsections we introduced the theory of TPE and SHG and we have shown their dependence on the square intensity of the electric field I^2. When the first experiment on those phenomena started it was not possible to use those techniques for studies on biological tissues, since high spatial and temporal density of photons are required. With the development of femto-second pulsed lasers the problem was solved and the first multi-photon microscope was then realized in 1990 by Denk, Strickler and Webb [7]

Beside TPE microscopy, in these last years SHG microscopy became an important tool for imaging of cells [23], cell membranes [42], tissues and in particular collagen fibers inside connective tissue [43].

In order to study the resolution of a two-photon microscope we consider our laser, with a wavelength λ and a perfect TEM_{00} beam, focused on the sample through an objective lens with numerical aperture NA. Since we are interested in axial and radial resolution, we rewrite the intensity distributions in cylindrical coordinates $I(\rho)$ and $I(z)$ by using two adimensional coordinates u and v, linearly dependent in ρ and z, defined by the following transformation:

$$v = \frac{2\pi(NA)\rho}{\lambda} \tag{2.52}$$

$$u = \frac{2\pi(NA)^2 z}{n\lambda} \tag{2.53}$$

where n is the refractive index of the medium. The electric field amplitude in these new coordinates is

$$E(u,v) = 2E_0 \int_0^1 J_0(v\rho)exp(-i\frac{\rho^2 u}{2})\rho d\rho \tag{2.54}$$

where J_0 is the zero order Bessel function of the first type. The field intensity is just the square of the electric field

$$I(v,u) = I(\rho,z) = |E(v,u)|^2 \tag{2.55}$$

As we said before, our interest is concentrated in the axial and radial intensity distribution, we can then study separately the two distributions at the objective focus. For $v = 0$:

$$|E(0, u)| = \left| 2E_0 \int_0^1 exp\left(-i\frac{u\rho^2}{2}\right) \rho d\rho \right|^2 \tag{2.56}$$

and for $u = 0$

$$|E(v, 0)| = \left| 2E_0 \int_0^1 J_0(v\rho)\rho d\rho \right|^2 \tag{2.57}$$

solving the integrals it is possible to obtain the following expressions

$$|E(0, u)|^2 = \left| E_0 \frac{\sin(u/4)}{u/4} \right|^2 \tag{2.58}$$

$$|E(v, 0)|^2 = \left| E_0 \frac{2J_1(v))}{v} \right|^2 \tag{2.59}$$

Since the transition probability in TPE and SHG is proportional to I^2, the axial and radial point spread functions (PSF_r and PSF_a), in case of TPE and SHG, are easily obtained by squaring the previous formulas, dividing first by $I_0 = E_0^2$.

$$PSF_a = \left| \frac{sin(u/4)}{u/4} \right|^4 \tag{2.60}$$

$$PSF_r = \left| \frac{2J_1(v)}{v} \right|^4 \tag{2.61}$$

An example of theoretical point spread function for a two-photon microscope with a 0.9 NA objective and 740 nm excitation wavelength is shown in Fig.2.1.

2.1.4   Conclusion

In this section we introduced the interaction between light and matter. We found first the probability of one photon transition, then we shown the quadratic dependence of TPEF and SHG with the field intensity and its
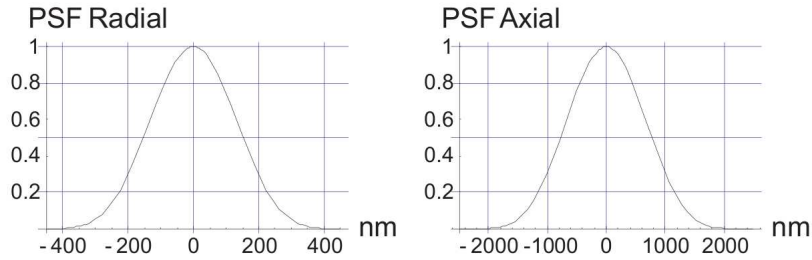
Figure 2.1: Point spread function of a two-photon microscope with a 0.9 NA objective and 740 nm excitation wavelength.

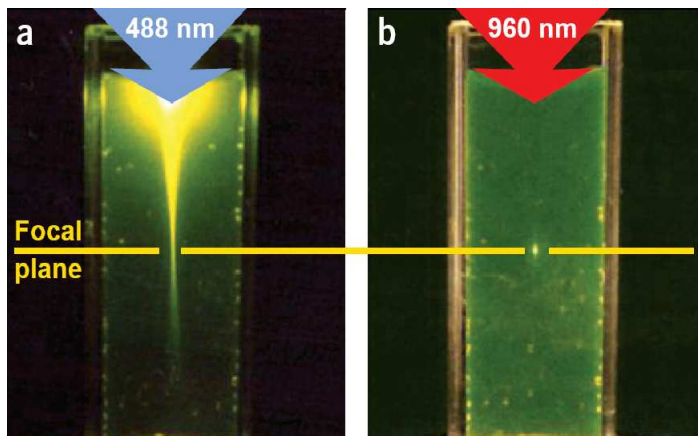involvement on the spatial resolution of the two-photon microscope.

Figure 2.2: Comparison between excitation volume in a fluorescein cuvette using single-photon excitation at 488nm, (a) and using two-photon excitation at 960nm (b)[9].

Considering the properties of the PSF and looking at Fig.2.2 it is easy to describe which are the main advantages of two-photon microscopy in comparison to confocal microscopy. Since the excitation occurs only on the focal plane, there is no need of a pin-hole. Moreover the photobleaching is highly reduced and the biological tissue is less exposed. Therefore two-photon microscopy is more suitable for *in vivo* application. A comparison between

excitation volume in two-photon microscope and excitation volume in single-photon confocal microscope is shown in Fig.2.2.

Furthermore, two-photon microscopy is well-suited for deep tissue investigations. In fact, Ti:Sa lasers used in two-photon microscopes have emission wavelengths in the the range of 700 nm -1000 nm, where biological tissues exhibit low absorption, as it can be seen in Fig.2.3.
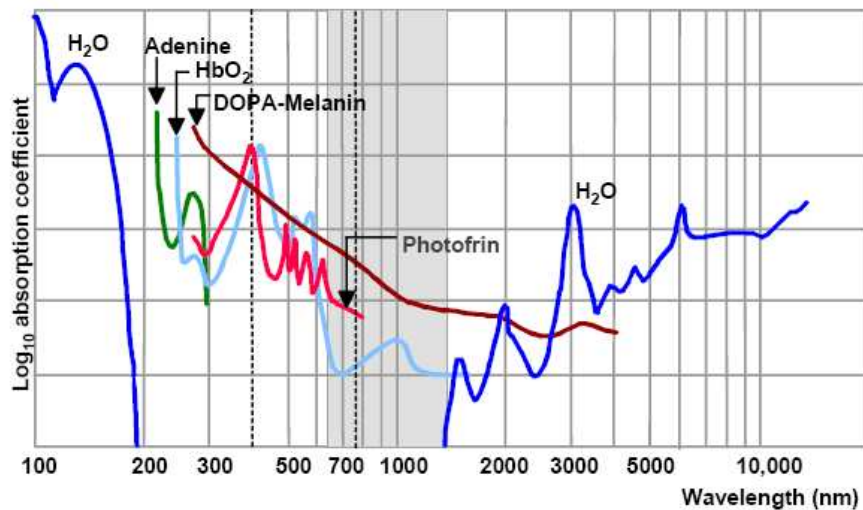

Figure 2.3: Absorption spectra of different endogenous molecules of biological tissues [44].

Besides TPEF, SHG microscopy is a powerful tool for imaging collagen, one of the main components of connective tissues, as skin dermis, that exhibts fibrillar structure and high hyperpolarizability. Finally, as it could be easily understood by looking at Fig.2.4, many endogenous molecules have similar two-photon cross section in the IR range, hence more molecules can be excited with the same wavelength.
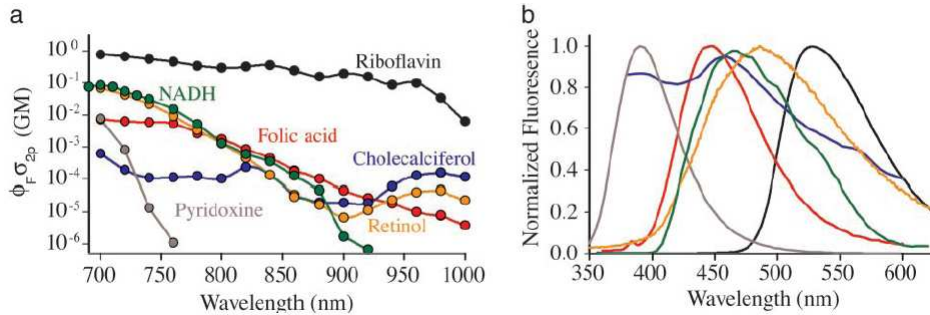
Figure 2.4: Cross section of different endogenous molecules of human tissues.

2.2 Fluorescence Lifetime Imaging Microscopy (FLIM)

The fluorescence lifetime of a molecule is defined as the average time that the molecule spends in the excited state before decaying, by fluorescence emission, back to the ground state. The determination of molecular fluorescence lifetime yield to important information on biological tissues[45, 46], as oxygen concentration, ionic strength, metabolism and proximity of other molecules. First measurements on molecular lifetime were made by Gaviola[47] in 1927, but the technique was well established for biological molecules at the end of the 80's [48, 49]. New improvements on the beginning of the 90's gave rise to the technique of fluorescence lifetime imaging microscopy (FLIM), where in the acquired image for each pixel it is possible to obtain both intensity, spectral and lifetime information. FLIM has been demonstrated using widefield [48], confocal [50] and also multiphoton microscopy[51].

There are two main FLIM techniques[52]: time-domain and frequency-domain. In this thesis both methods were employed. The former, that was used in the two-photon microscope, uses high frequency pulsed laser, with a pulse time width of few hundreds fs, and fast electronics for single photon counting. It is based on the time distribution of the fluorescence photon arrival time after several exciting pulses.

The latter was used in the fiber probe and it uses intensity modulated sources. It consists on the determination of the phase shift and modulation amplitude

of the fluorescence intensity with respect to the modulated laser excitation intensity.

2.2.1 Fluorescence lifetime

Let's consider an ensemble of N_0 excited molecules after an indefinetely short pulse of light, their decay rate can be written as

$$\frac{dN(t)}{dt} = -(\Gamma + \kappa)N(t) \tag{2.62}$$

where Γ and κ are the radiative and non-radiative decay rates and $N(t)$ is the number of molecules in the excited state. Setting $N(0) = N_0$ and integrating we obtain

$$N(t) = N_0 exp\left(-\frac{t}{\tau}\right) \tag{2.63}$$

where

$$\tau = \frac{1}{\Gamma + \kappa} \tag{2.64}$$

is defined as the lifetime of the excited state. We can then expect the fluorescence intensity $I(t)$ to decay exponentially, since it is proportional to the population of the excited molecules. In a more general way, the lifetime of the excited state can be defined as the ensemble-averaged time that the population remains in the excited state

$$\langle t \rangle = \frac{\int_o^\infty tN(t)dt}{\int_o^\infty N(t)dt} \tag{2.65}$$

which, in case of an exponential decay, becomes

$$\langle t \rangle = \frac{\int_o^\infty tN_0 exp\left(-\frac{t}{\tau}\right)dt}{\int_o^\infty N_0 exp\left(-\frac{t}{\tau}\right)dt} \tag{2.66}$$

obtaining

$$\langle t \rangle = \tau \tag{2.67}$$

Therefore the lifetime can be defined as the average time one molecule spend in the the excited state before decaying, by fluorescence emission, back to

the ground state.

2.2.2   Time domain FLIM

The most common measurement technique in the time domain FLIM is the time-correlated single photon counting (TCSPC), where for each exciting pulse the arrival time of the fluorescence photon is recorded. By exponential fitting on the photon arrival time distribution it is possible to calculate the lifetime τ.

Let's divide the repetition period T_r of the excitation pulses in N_t time channel of amplitude Δt. We define the time channel i as the time period ranging from $i \cdot \Delta t$ and $(i+1) \cdot \Delta t$, with $i < N_t$. The average number of fluorescence photons recorded in the time channel i after one excitation pulse is

$$\overline{x}_i = \overline{n}_i q \tag{2.68}$$

where $\overline{n}_i$ is the number of photons reaching the detector at the time channel i and q is the quantum efficiency. After several excitation pulses the probability distribution $P_x(i)$ to reveal x photons in the ith channel is a Poisson distribution defined as

$$P_x(i) = \frac{(\overline{x}_i)^x exp(-\overline{x}_i)}{x!} \tag{2.69}$$

with the condition

$$\sum_{x=0}^{\infty} P_x(i) = 1 \tag{2.70}$$

If we consider then the probability to have at least one photon detected:

$$P_{x \geq 1}(i) = 1 - P_0(i) = 1 - exp(-\overline{x}_i) = 1 - \left(1 - \overline{x}_i + \frac{\overline{x}_i^2}{2} + \cdots \right) \tag{2.71}$$

For very low light intensity $\overline{x}_i \gg \overline{x}_i^2/2$ we obtain

$$P_{x \geq 1}(i) \simeq \overline{x}_i = \overline{n}_i q \tag{2.72}$$

Therefore, under this condition there is a linear proportionality between the probability of detecting one or more photon per excitation pulse in the time channel i and the fluorescence intensity at time t_i. This condition, required for an accurate TCSPC measurement, could be expressed also by the following expression

$$\frac{R_d}{R_s} = \alpha \ll 1 \tag{2.73}$$

where R_s is the source repetition rate and R_d is the total rate of the the detected fluorescence photons over all the delay times. Typically it is required a value $\alpha \leq 0.01$, so that the probability of detecting more then one photon per excitation pulse is negligible.

Using femtosecond laser pulses, the excitation could be assumed as a δ-function. In case of single-exponential decay of fluorescence with lifetime τ, the number of photons counted Y_i per time channel i during a measurement time T is given by

$$Y_i = \alpha R_s T \frac{\Delta t}{\tau} exp\left(-\frac{i\Delta t}{\tau}\right) \tag{2.74}$$

Hence, the enhancement of the statistics of the photon arrival time, and therefore the measurement precision, can be improved by increasing the acquisition time T.

TCSPC time resolution

Even if the output pulse from the laser is of the order of $100fs$ (as in the case of Ti:Sa laser) the excitation pulse measured by the electronic detection system is not a true δ-function but it will result broader due to different broadning source as

- Microscope Optical Components

- The detector response

- The timing electronics

The instrumental response function (IRF) $R(t)$ is then the convolution product between the temporal profile of the excitation pulse $S(t)$ and the impulse

response of each broadning source

$$R(t) = S(t) \otimes O(t) \otimes D(t) \otimes E(t) \tag{2.75}$$

where $O(t)$, $D(t)$ and $E(t)$ are respectively the impulse response function of the optical components, the detector and the electronics. The effective measured FWHM time width of the excitation pulse Δt_m could be written as

$$\Delta t_m \simeq \left[(\Delta t_e)^2 + \sum_i (\Delta t_i)^2 \right]^{\frac{1}{2}} \tag{2.76}$$

where Δt_i is the FWHM of the impulse response of the component i and Δt_e is the FWHM of the excitation pulse.

Even if the measured instrumental pulse Δt_m is greater then the lifetime to be measured, it is still possible to evaluate the theoretical fluorescence response $I(t)$. In fact, the fluorescence decay signal $F(t)$ can be expressed as the convolution between the IRF and the theoretical fluorescence response for δ excitation pulse

$$F(t) = \int_0^t R(t')I(t - t')dt' \tag{2.77}$$

Therefore, by de-convoluting the instrumental response function $R(t)$, from the fluorescence decay signal $F(t)$ it is possible to extract $I(t)$. Then, by fitting using an exponential decay function we can calculate the value of the lifetime τ.

2.2.3 Frequency domain FLIM

Time-domain FLIM is a powerful method to measure the lifetime of a molecule but it needs a pulsed laser source and fast electronics. In frequency-domain FLIM the intensity of the light source is modulated on the order of 10-100 MHZ. The fluorescence signal, in case of single-photon transition, is proportional to the excitation intensity and thus has the same frequency, but it is shifted by a phase factor δ. Moreover its modulation ratio will be lower since

the decay time of the excited molecules is not instantaneous. The method of frequency domain FLIM was invented by Gaviola in 1927 [47], and the theory was given in detail by Dushinsky [53] in 1933. Further improvement where introduced by Spencer and Weber [54, 55].

Let's take for simplicity a homogeneus solution, in which a single fluorophore with a single exponential decay is excited by a sinusoidal modulated laser source $E(t) = A + Bcos(2\pi f_{ex}t)$. The expression for the fluorescence signal $F(t)$ is given by the convolution product of the source term with the impulse response of the emission process:

$$F(t) = [A + Bcos(2\pi f_{ex}t] \otimes e^{-\frac{t}{\tau}} = A + B\cos\delta\cos\left(2\pi f_{ex}t - \delta\right) \qquad (2.78)$$

where

$$\tan\delta = 2\pi f_{ex}\tau \qquad (2.79)$$

We can write the relative modulation M, defined as the modulation ratio of fluorescence divided by the modulation ratio of the excitation, as follows:

$$M = \cos\delta = \frac{1}{\sqrt{1 + 4\pi^2 f_{ex}^2\tau^2}} \qquad (2.80)$$

Therefore the lifetime τ can be calculated either by measuring the phase shift δ or by measuring the relative modulation M. By inverting the formulas above, obtaining respectively values of lifetime τ^δ and τ^M, for single fluorophore we have:

$$\tau^\delta = \tau^M \qquad (2.81)$$

In Fig.2.5 are shown the The fluorescence signals in comparison with the laser excitation intensity in case of short and long lifetime with respect to the excitation period defined as $2\pi/f_{ex}$, are shown in Fig.2.5.

Resolution of the fluorescence lifetimes in heterogeneus systems

For a single fluorophore with a single-exponential decay the lifetime measurement is relatively easy, but if we have a heterogeneus system with more than
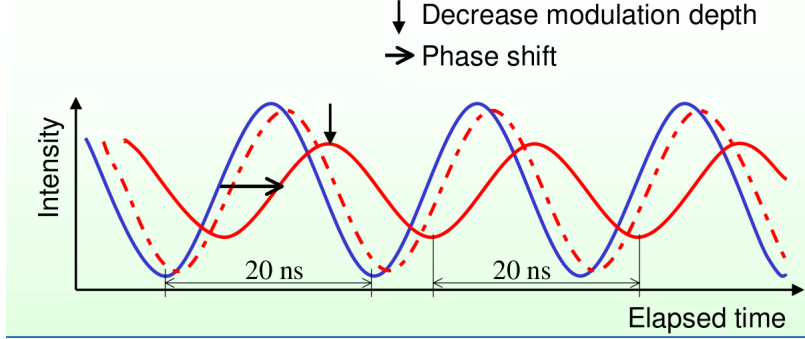
Figure 2.5: Laser excitation intensity modulation, in blue, and fluorescence signal for short lifetime, dashed, and for long lifetime, red

one fluorophore the measurement is getting more complicated and more than one modulation frequency is required[55]. Let's suppose to have a heterogeneus system with N fluorophores excited with a frequency f. The fluorescence signal on the detector can still be expressed as $A + B \cos \delta \cos (2\pi f t - \delta)$, but in this general case:

$$\tan \delta = \frac{\sum_i^N \epsilon_i \sin \delta_i}{\sum_i^N \epsilon_i \cos \delta_i} \tag{2.82}$$

$$M^2 = \left(\sum_i^N \epsilon_i \sin \delta_i \right)^2 + \left(\sum_i^N \epsilon_i \cos \delta_i \right)^2 \tag{2.83}$$

where δ_i is the phase shift contribution of each fluorophore and ϵ_i is defined as

$$\epsilon_i = F_i \cos \delta_i \tag{2.84}$$

where F_i is the fraction of the total fluorescence intensity due to the ith fluorophore. By defining

$$G = \sum_i^N F_i \cos^2 \delta_i \tag{2.85}$$

$$S = \sum_i^N F_i \cos \delta_i \sin \delta_i \tag{2.86}$$

we can give a new expression for

$$\tan \delta \;=\; S/G \tag{2.87}$$

$$M^2 \;=\; S^2 + G^2 \tag{2.88}$$

If we modulate at a frequency f_r, by using eq.(2.79) and eq.(2.80), we would obtain an "apparent lifetime by phase" τ_r^δ and an "apparent lifetime by modulation" τ_r^M. The combination of their expression with eq.(2.88) and eq.(2.87) yields

$$G_r \;=\; M_r \cos \delta_r = \left[(1 + (2\pi f_r \tau_r^\delta)^2)(1 + (2\pi f_r \tau_r^M)^2)\right] \tag{2.89}$$

$$S_r \;=\; M_r \sin \delta_r = G_r 2\pi f_r \tau_r^\delta \tag{2.90}$$

Let's consider the general case where we would like to determine N independent lifetimes $\tau_1 \ldots \tau_N$ and N fluorescence contribution factor $F_1 \ldots F_N$. By exciting at N different frequencies it is possible to determine all the values of τ_i and F_i of each individual component. In fact, supposing to use N harmonics f_r of a base frequency f_0 and calling

$$p_r \;=\; f_r/f_0 \tag{2.91}$$

$$a_i \;=\; f_0 \tau_i \tag{2.92}$$

we can finally write

$$G_r \;=\; \sum_i^N (1 + p_r^2 a_i^2)^{-1} \tag{2.93}$$

$$S_r \;=\; \sum_i^N F_i p_i a_i (1 + p_r^2 a_i^2)^{-1} \tag{2.94}$$

As a result of the observation at N different excitation frequencyies, we obtain N measurements of G and S. Therefore we can determine the first $2N$ moments, from zero order to $2N - 1$, of the distribution of the a_i values. It is easy to notice that the zero and the even moments arise from linear combination of the N values of G, while the odd moments arise from linear

combination of the N values of S.

In case of a heterogeneous solution of two fluorophores, in order to calculate the two lifetimes and the fractional intensities, two excitation harmonics are required. The two fractional intensities are normalized, therefore $F_1+F_2 = 1$. The moments of the distribution of lifetimes can be expressed as

$$m_0 = p_1^2 G_1 - p_2^2 G_2 \tag{2.95}$$

$$m_1 = p_1 S_1 - p_2 S_2 \tag{2.96}$$

$$m_2 = -G_1 + G_2 \tag{2.97}$$

$$m_3 = -S_1/p_1 + S_2/p_2 \tag{2.98}$$

and by defining $\Delta = m_2 m_0 - m_1^2$ and

$$\Theta_1 = (m_3 m_0 - m_2 m_1)/\Delta \tag{2.99}$$

$$\Theta_2 = (m_3 m_1 - m_2^2)/\Delta \tag{2.100}$$

we can give the following expression for a_1 and a_2

$$a_{1,2} = \frac{\Theta_1}{2} \pm \left(\frac{\Theta_1^2}{4} - \Theta_2 \right) \tag{2.101}$$

from which we can calculate easily τ_1 and τ_2 by diving for $2\pi f_0$. The relative intensities of the components are defined as follows:

$$F_2 = G_1 - \frac{(1 + p_1^2 a_1^2)^{-1}}{[(1 + p_1^2 a_2^2)^{-1} - (1 + p_1^2 a_1^2)^{-1}]} \tag{2.102}$$

$$F_1 = 1 - F_2 \tag{2.103}$$

2.2.4 Digital Frequency Domain FLIM

The FLIM techniques described above are really well-established and have good precision and sensitivity, but they present some disadvanteges. For TC-SPC the main disadvantages are due to high cost of electronics and difficult lifetime analysis on many pixel simultaneously. Besides, frequency domain FLIM (FD-FLIM) requires radio frequency (RF) gain modulated detectors

and therefore it does not operate at full gain.

In the last years a new technique for lifetime determination was developed by Gratton and Colyer [56]. In this method the signal out from the detector is digitized and the heterodyning occurs digitally on a field programmable gate array (FPGA) chip. Therefore it is called Digital Frequency Domain FLIM (DFD FLIM).

In this technique a sampling frequency f_s is generated in order to be slightly higher then the excitation frequency f_{ex}. The sampling frequency is then used to gate the photon arrival on a time period Δt_G that is a whole integer fraction of the excitation period Δt_{ex}. The resulting cross correlation frequency $f_{cc} = f_s - f_{ex}$ will sample all the possible phases of the decay fluorescence signal detected.

In order to understand better this method, let's use the image in fig.2.6. Supposing a pulsed excitation, it will be easy to generalize to the case of digital modulation excitation intensity. On the top of the figure it is shown the decay profile of the fluorescence. If we then consider the first sampling window, numbered as "0", the first time gate is in phase with the excitation source and it will sample the first part of the decay profile. The following time gates generated at a frequency f_s will contain all the possible phases of the decay profile. After a time period Δt_{cc}, defined as the own period of f_{cc}, the time gate will be once again in phase with the excitation pulse. By using four sampling windows and $\Delta t_G = \Delta t_{ex}/4$ is then possible to have 100% duty cycle.

DFD-FLIM theory

In DFD-FLIM the excitation could be performed by both pulsed and digital intensity modulated sources. In this second case the advantage is the possibility of recording two or more harmonics in the same acquisition. In order to determine the contribution of each component to the lifetime measurement,
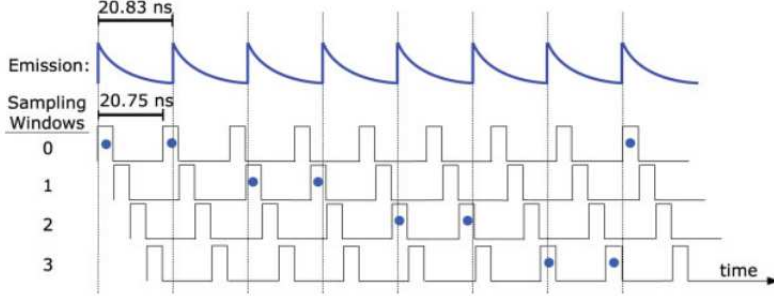
Figure 2.6: Illustration for description of digital heterodyning[56]. For simplicity $f_{cc} = f_s/8$, in this case the sampling window contains 8 different phases of the decay profile. The dots represent the photon arrival times.

we can then expand them in Fourier series. For the excitation we have

$$E(t) = 1 + \sum_h 2m_{E,h} \cos\left(2\pi h f_{ex} t - \delta_{E,h}\right) \tag{2.104}$$

where we defined $2m_{E,h}$ as the modulation of the excitation at each harmonic and $\delta_{E,h}$ an arbitrary phase shift. The fluorescence response of an arbitrary combination of fluorophores can be expressed as

$$
\begin{aligned}
F(t) &= f_o + \sum_i \left(\frac{F_i}{\tau_i(1 - exp(-1/(f_{ex}\tau_i)))}\right) e^{-t/\tau_i} = \\
&= 1 + \sum_h 2m_{F,h} \cos\left(2\pi h f_{ex} t - \delta_{F,h}\right)
\end{aligned}
\tag{2.105}
$$

where τ_i are the fluorescence lifetimes, f_o is the contribution of uncorrelated background and F_i the fractional intensity. It is then possible to take into account the response jitter, assumed as Gaussian, due to the detector, the discriminator and the logic gate.

$$J(t) = \frac{1}{\sigma_j \sqrt{(2\pi)}} e^{(-t^2/2\sigma_i^2)} = 1 + \sum_h 2m_{J,h} \cos\left(2\pi h f_{ex} t - \delta_{J,h}\right) \tag{2.106}$$

where σ_j is the standard deviation of the detection time jitter, including all the components in the detection system. Considering one of the n_W arrival

windows, each of them is shaped as a periodic boxcar function

$$S(t) = \begin{pmatrix} f_s \ if \ \left(\frac{w_{arrival}}{n_w f_s}\right) \leqslant \left(t \ mod \frac{1}{f_s}\right) \leqslant \left(\frac{w_{arrival+1}}{n_w f_s}\right) \\ 0 \ otherwise \end{pmatrix}$$
$$= 1 + \sum_h 2m_{S,h} \cos\left(2\pi h f_s t - \delta_{S,h}\right) \tag{2.107}$$

where $n_{arrival}$ is the index of the arrival time window, ranging from 0 to n_W -1, and f_s is the sampling frequency.

The probability distribution of the detected photon can be evaluated by simply convoluting the excitation, the fluorescence response, the jitter of the system and the sampling window

$$H(t) = E(t) \otimes F(T) \otimes J(t) \otimes S(t) \tag{2.108}$$

We can finally write $H(t)$ expanded in Fourier series

$$H(t) = 1 + \sum_h 2m_{E,h} m_{F,h} m_{J,h} m_{S,h} \cos\left(2\pi h f_{cc} t - \left((\delta_{S,h} - \delta_{E,h}) + \delta_{F,h}\right)\right) \tag{2.109}$$

Since $E(t)$ and $S(t)$ have two different frequency, the frequency of $H(t)$ is actually the cross correlation frequency defined as

$$f_{cc} = |f_{ex} - f_s| \tag{2.110}$$

Finally we can write the modulation of $H(t)$ at each harmonic h as the product of all the modulation components

$$m_{H,h} = m_{E,h} m_{F,h} m_{J,h} m_{S,h} = m_{F,h} m_{IR,h} \tag{2.111}$$

where $m_{IR,h}$ represents the whole contribution by all the instrument components. About the phase shift, it can be expressed as

$$\delta_{H,h} = (\delta_{S,h} - \delta_{E,h}) - \delta_{F,h} = \delta_{F,h} + \delta_{IR,h} \tag{2.112}$$

where we defined $\delta_{IR,h} = (\delta_{S,h} - \delta_{E,h})$. $\delta_{IR,h}$ can be evaluated by using a standard fluorophore with known lifetime for calibration.

2.2.5 Conclusion

In this section we introduced fluorescence lifetime imaging microscopy and the different techniques that are used in order to determine the lifetime of molecules. As we said, TCSPC and frequency domain FLIM (FD-FLIM) have some disadvantages: cost and calculation complexity for the former, requirement of radio frequency (RF) gain modulated detectors and RF amplifier electronic for the latter. DFD-FLIM is a relatively cheap techniques and can be used both with pulsed and modulated excitation, with 100% duty cycle. Furthermore in case of digital modulation it is possible to acquire simultaneously more harmonics. In this thesis both methods, TCSPC and DFD-FLIM were used.

Chapter 3

Experimental set-up

In these 3 years of PhD I made measurements on human samples by using two different experimental set-ups. Most of my project has involved a custom-built two-photon microscope I used for analysis on healthy and tumoral fresh biopsies of bladder and for studies on a dermatological disorder of dermis. Beside I built an optical fiber probe for fluorescence spectroscopy and lifetime measurements with endoscopic capability. In this part I'm going to describe and characterize both set-ups.

3.1 Two-photon microscope

3.1.1 Experimental set-up

The experimental set-up I used is a custom-made two-photon microscope built on a vertical honeycomb steel breadboard. A sketch of the microscope is shown in Fig.3.1. The laser source is a mode-locked Ti:Sapphire laser Chameleon Ultra II (Coherent Inc, Santa Clara, CA, US) providing pulsed illumination with 140 fs pulse length at a repetition rate of 80 MHz. The laser driver allows to tune the emission wavelength from 680 nm up to 1080 nm. A telescope, indicated as L1 and L2, is used for collimating the laser beam. The beam power is adjusted by using a motorized rotating half-waveplate followed
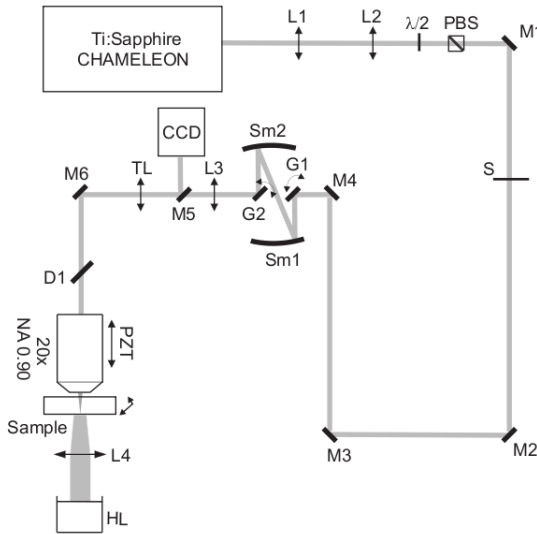
Figure 3.1: Scheme of the two-photon microscope

by a polarizing beam-splitter cube (PBS). The scanning system is composed by two galvo-mirrors (G1,G2) VM500 (GSI Lumonics, Munich, Germany) coupled by two spherical mirror (Sm1 and Sm2). The two galvo-mirrors are placed in the conjugate planes of the objective back focal plane and they are driven by an I/O board PCI-MIO-16E (National Instruments, Austin, TX, US). The laser beam is then expanded to the diameter of around 1 cm through a telescope, constituted by the scanning lens (L3, f = 50 mm) and the tube lens (TL, f = 200 mm). Finally it is focused onto the sample by an objective XLUM 20x, N.A. 0.90, W.D. 2 mm (Olympus Co., Japan). By using a piezo-electric stage (PZT) PIFOC P-721 (Physik Instrumente GmbH, Karlsruhe, Germany) it is possible to scan the specimen along the vertical axis with sub-nanometer resolution and up to 100 μm maximum displacement. The TPE and SHG signals are collected by the objective and reflected by a dichroic filter (D1) 685DCXRU (Chroma Technology Corporation, Rockingham, VT, US) with 685 nm cut-off wavelength placed immediately behind the objective lens.

In order to prevent any unwanted back-reflection of the laser to be detected, a two-photon cut off filter (SBF) E700SP-2P (Chroma Technology Corporation, Rockingham, VT, US) is inserted in the detection path. The light

passes through a lens (L5) and then it is focused into the sensitive areas of two photomultiplier tubes (H9503, Hamamatsu, Japan). In order to have a simultaneous acquisition of two-photon fluorescence and second-harmonic generation when using 840 nm as excitation wavelength, a separating dichroic mirror with 457 nm cut-off wavelength (DC457LP Semrock, Rochester, NY, US) is placed in the detection path. Both PMTs, together with the second dichroic, are mounted on a removable magnetic stage. A sketch of the detection system is shown in Fig.3.2.

A narrow pass-band filter (BF) (HO420BP, Chroma Technology Corporation, Rockingham, VT, US) is placed in front of the SHG detector in order to remove any fluorescence contribution from the SHG signal. The signals coming out from the PMTs are first amplified by a custom-built amplification stage and then acquired by the I/O board.
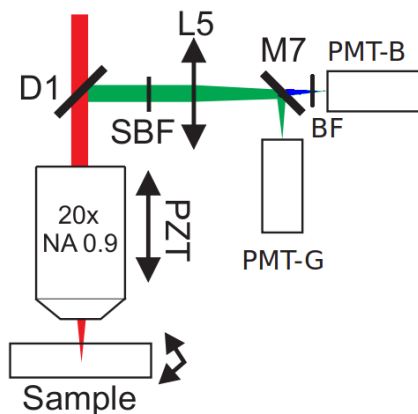

Figure 3.2: Scheme of the detection system

Image acquisition and formation

System acquisition is controlled through a Labview program which is responsible to synchronize the scanning operation with the detection and to reconstruct the image. For each illuminated pixel the corresponding fluorescence signal is acquired by means of a trigger provided by the scan clock.
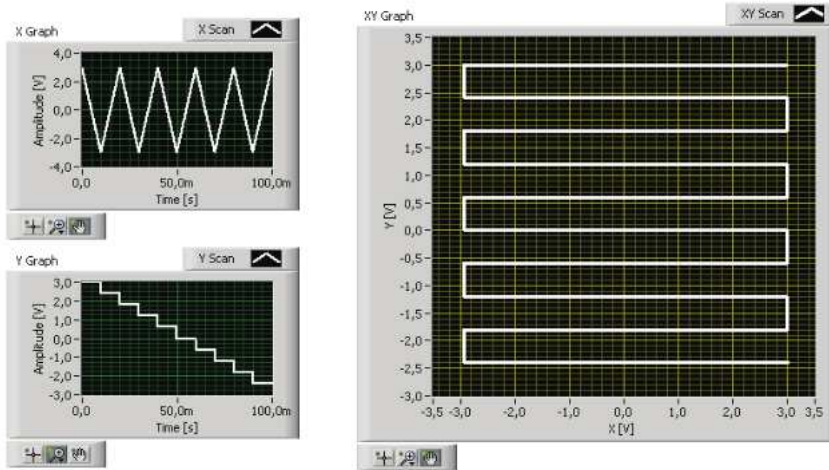
Figure 3.3: Sketch of the raster scanning program waveform. On the left the two scanning waveform for X axis (top) and for Y axis (bottom). On the right the combined XY waveform.

The software generates two waveforms, as shown in Fig.3.3: one triangular wave for the X axis and one linear decreasing ramp for the Y axis. The combined XY waveform is the raster graph in Fig.3.3. The program accepts different inputs, as the scan rate (its inverse correspond to the pixel dwell time), the number of X pixels and Y pixels, the X and Y amplitude (corresponding to the field of view dimension on each axis). The Z scan is driven by a piezoelectric stage. The program allocates three memory buffers of the same dimensions (corresponding to the data dimensions of the image to be acquired): one for the analog output control of the galvo-mirrors one, two for the two analog inputs from the two photomultipliers. A trigger line is configured for simultaneously starting the I/O, then the acquisition occurs at a rate corresponding to the scanning rate.

3.1.2 Spatial calibration and microscope resolution

Raster scanning in the XY plane is performed by driving the galvo-mirrors with the waveforms described in the previous paragraph. Galvo-mirrors are

driven through a voltage in the range of $\pm$ 10 V. The spatial calibration consists in determining a V/μm conversion factor in order to have a correspondence between galvo deflection in volts and beam position in the focal plane in μm. The spatial calibration was accomplished through a graded microscope slide. The calibration was done by varying the voltage on the galvo-mirrors until the field of view corresponds to 100 μm in the graded microscope slide, then it is possible to calculate the conversion factor. We verified the linearity between the voltage applied to galvo-mirrors and the linear dimension of the field of view in the focal plane.

Since two-photon absorption is a non-linear effect, the spatial resolution of the microscope is smaller than the beam waist. The spatial resolution corresponds to the dimension of the excitation volume, hence it can be measured by using a fluorescent object with dimensions much smaller than the expected resolution. For this reason, in order to measure the microscope resolution in the XY plane and along the optical axis, we imaged quantum dots of about 20 nm diameter (Q10121MP Invitrogen Corporation, Carlsbad, CA, US), which is more than one order of magnitude below the diffraction limit of the microscope. Spatial resolution is then evaluated by measuring the FWHM of the PSF. A stack of images of a single quantum dot at different positions along the optical axis is shown in Fig.3.4.
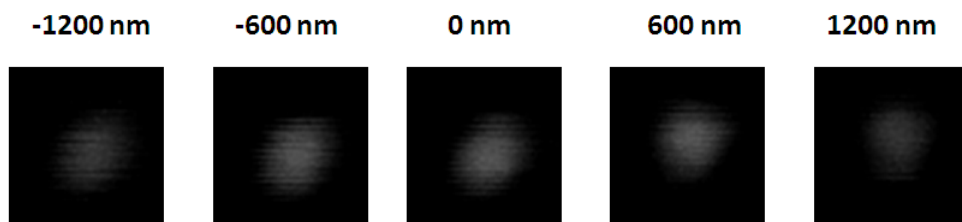

Figure 3.4: Stack of images of a single quantum dot at different positions along the optical axis. The images have a dimension of 4 μm, the depth is indicated above. Measurement of spatial resolution were accomplished with a 60x objective, NA 1.2 and using water as immersion medium (n=1.33).

The measurement of spatial resolution was accomplished by using a 60x objective, NA 1.2 and using water as immersion medium (n=1.33). A microscope slide was prepared with a solution of water and q-dots at low concentration in order to have in average less than one q-dot per field of view, in our case 4 μm. Considering an acquisition of 512x512 pixels, the scanning resolution is 16 nm in the XY plane. A stack of images along the optical axis was realized with a scanning resolution of 100 nm. We found a radial resolution of 300 nm and an axial resolution of 1400 nm, using an excitation wavelength of 900 nm (Fig.3.5).
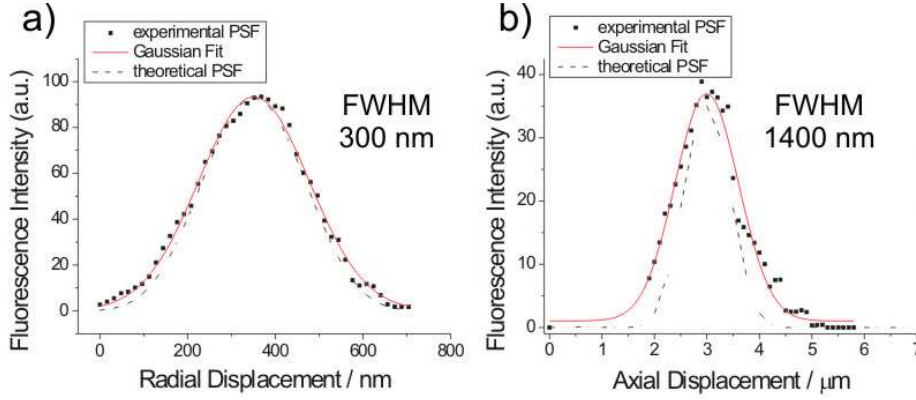

Figure 3.5: Point Spread Function (PSF) of the quantum dot in the XY plane and along the optical axis. The dots are indicating the experimental data, the dotted line the theoretical value and the red line the Gaussian fit on experimental data. Measurement of spatial resolution were accomplished with a 60x objective, NA 1.2, using water as immersion medium (n=1.33) and an excitation wavelength of 900 nm.

3.1.3   FLIM detection system

The experimental set-up is equipped with a second detection system based on photon counting regime for FLIM acquisition. In order to acquire FLIM images the magnetic stage with the two PMTs must be removed. In this configuration fluorescent light is sent, after being reflected by a mirror, to an

objective lens Plan 10x, 0.25 NA (Nikon, Tokyo, Japan) and then coupled to a 900 μm core diameter multi mode optical fiber (OF).
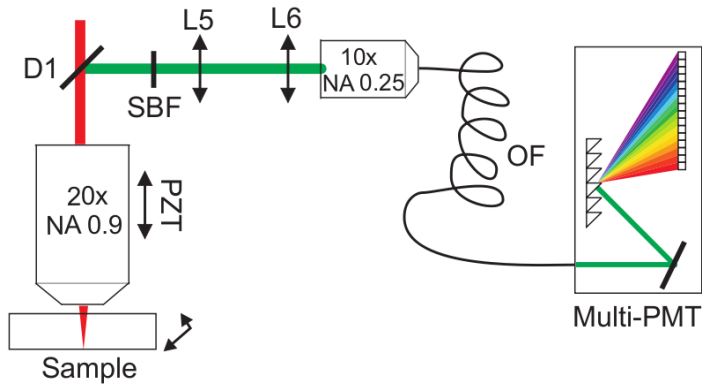

Figure 3.6: Scheme of the FLIM detection system

The fiber ends at the entrance slit of a spectrometer. Light passes through a diffraction grating and is revealed by a 16-channels multi-anode photomultiplier strip (Multi-PMT) PML-Spec (Becker&Hickl GmbH, Berlin, Germany) with 250 ps FWHM pulses. Time-resolved measurements on each spectral channel, corresponding to each channel of the strip, are made by a I/O board SPC-730 (Becker&Hickl GmbH, Berlin, Germany). A labview program drives an electronic timing board E-6502 (National Instruments, Austin, TX, US) allowing synchronization between the SPC-730 and the National Instruments I/O board. The SPC-730 photon counting board settings are controlled by means of a dedicated software SPCM 1.1 (Becker&Hickl GmbH, Berlin, Germany). Acquired images are visualized and analyzed by using the software SPC Image 2.8 (Becker&Hickl GmbH, Berlin, Germany).

3.1.4 Detection principle

Typical values of fluorescence lifetime of molecules in biological tissues are ranging from 0.5 ns up to 4 ns. Hence, it is not possible to perform accurate lifetime measurements by normal sampling of the fluorescence light intensity,

because of a too fast acquisition rate on extremely low light levels. High temporal resolution in lifetime determination can be achieved by using Time Correlated Single Photon Counting (TCSPC). The method, as described in the previous chapter, uses a periodic pulse excitation and makes a statistics on fluorescence photons arrival time. The excitation pulse triggers the start of a time to amplitude converter (TAC), the stop signal is given by the detection of a fluorescence photon. The event is recorded by adding one unit at the memory location with an address related to the corresponding time channel. After several excitation pulses a histogram distribution of the arrival time of detected photons is obtained. The operation is iterated for each pixel in the image, so that each pixel contains the information about a decay histogram that represents the fluorescence decay.
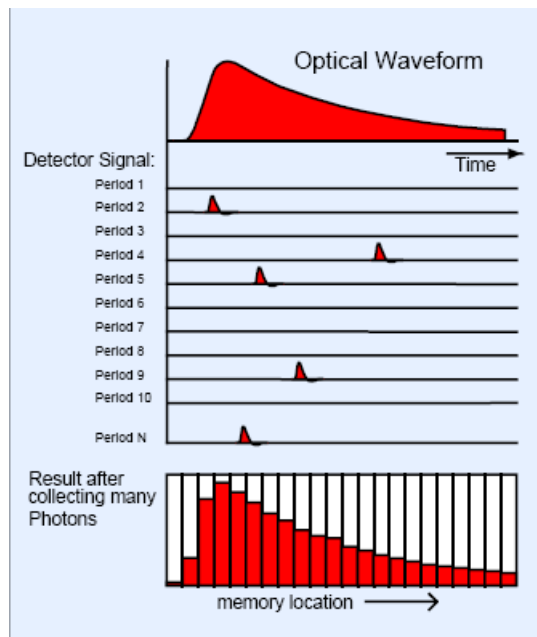

Figure 3.7: Detection principle for Time Correlated Single Photon Counting (TCSPC)

Images can be acquired with or without spectral information. In the former case the memory is divided in 16 blocks. Every block corresponds to 1 channel

of the PMT strip, therefore to a specific band of the spectrum with 13 nm width. In the latter case all the memory is devoted to acquire the arrival time of all photons, without information about the spectral channel. The memory of the board is limited to 16 MByte and data are stored in 16 bits resolution. Hence, the product of the number of pixels of the image, by the number of time channels, by the number of spectral channels can not exceed 8 M points. Spectral images must have a lower temporal or spatial resolution with respect to single channel acquisition, because of limited memory size.

3.1.5   Image analysis

Image analysis is performed by using SPC-Image 2.8 (Becker&Hickl GmbH, Berlin, Germany). As pointed out in the previous paragraph, for each pixel of the acquired image there is a decay histogram representing the number of photon arrived per time channel. Under the condition shown in eq.(2.73) there is a linear proportionality between photons counted in the time channel i and the fluorescence intensity at time t_i. Therefore, by deconvolving the histogram with the instrumental response function, it is possible to obtain the fluorescence decay curve which can be fitted with a single or multiple exponential decay function. In case of multispectral FLIM, 16 spectral images are obtained in parallel and both deconvolution and analysis have to be conducted on each spectral channel.

3.1.6   Time resolution

The instrument response function (IRF) was already introduced in the previous chapter. In eq.2.75 we considered the IRF as the the convolution product between the temporal profile of the excitation pulse $S(t)$ and the impulse response of each broadening source.

In order to measure the IRF we just removed the two-photon cut-off filter from the detection path and a small reflection of the excitation laser pulse was sent into the detector, after proper filtering (OD $>$ 4). The power was maintained at low levels in order to avoid saturation of the detector. Since the temporal FWHM of the laser pulse is barely 140 fs, we can assume it

as a δ-Dirac excitation in time. The output signal measured shows a 300 ps FWHM, in a good agreement with the 250 ps time response of the PMT. Further broadening can be due to additional broadening sources such as optics and electronics.
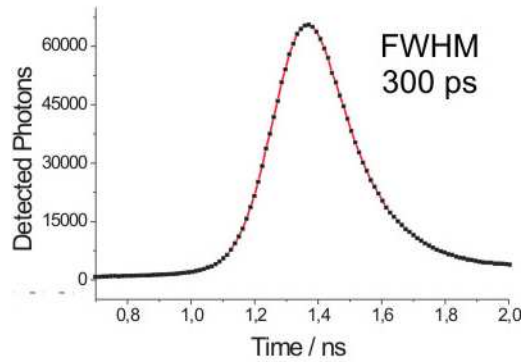

Figure 3.8: Measured IRF

3.2 Multi dimensional-purpose fiber probe

Part of my PhD work consisted in designing and realizing a fiber optical probe for *in vivo* measurement on skin or on internal organs, as bladder. The main features to be considered during the probe designing are a fast acquisition and high flexibility. Furthermore the fiber probe might have an outer diameter smaller than 3 mm in order to be used in a service channel of a commercial cystoscope. Even if single-photon microendoscopy is already a well-established technique used in many laboratories, and commercially available [57, 21], we decided to sacrifice imaging capability with the purpose of having short acquisition time and a simple technology. The probe is in fact able to detect spectral and lifetime information by exciting a small volume of tissue but it is not able to provide an image.

Fluorescence spectroscopy and lifetime should be able to provide a "chemical fingerprint" on the tissue under investigation[46, 40, 45]. An important

feature provided by spectral-lifetime measurements is the capability of measuring the balance between nicotinamide adenine dinucleotide (NADH) and flavin adenine dinucleotide (FAD). In fact, according to the Warburg effect [39], tumoral cells preferably switch to the glycolysis biochemical pathway in comparison with healthy cells in which phosphorylation dominates. In the former case only NADH is involved, while in the latter cells are using both NADH and FAD. Therefore, a higher NADH contribution is expected in tumoral cells [40]. Another important feature arises from fluorescence lifetime of endogenous molecules. By measuring both fast and slow components of the fluorescence decay of a molecule, it is possible to understand if the molecule is in its free or protein-bound state and hence, to have an information about cellular metabolism [46].

The fiber probe was designed in order to perform fluorescence spectroscopy and fluorescence lifetime measurements at 378 nm and 445 nm excitation wavelength. The two wavelengths used in our set-up were chosen in order to excite respectively NADH and FAD. In the future it will be completed with Raman spectroscopy.
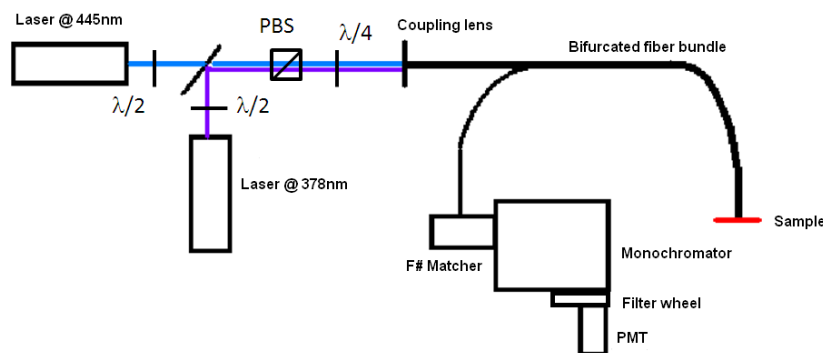
3.2.1 Fiber probe

Figure 3.9: Sketch of the optics of the fiber probe

Two laser sources at 378 nm and 445 nm (TEC42,Sacher Lasertechnik GmbH, Marburg, Germany) are coupled together through a dichroic mirror (FF409-Di02-25x36 ,Semrock, Rochester, NY, US) and delivered in the central fiber of a custom-made bifurcated fiber bundle (Ely-Prizmatix, Modiin Ilite, Israel). A polarizer cube (GTH10M, Thorlabs, Newton, NJ , US), followed by a quarter-waveplate (WPA1212-L/4-375-445, Casix, Fuzhou Fujian, China), is placed after the dichroic in order to block back reflection from the coupling fiber launcher. The laser power is maximized using two half-waveplates (WPO-12.7CQ-0-2-442 and WPO-12.7CQ-0-2-355,LAMBDA, Costa Mesa, CA, US), one for each laser.

On the distal end of the probe fibers are arranged in honey-comb configuration: there is a central delivering fiber (100μm core, High OH, NA 0.22), surrounded by 48 collecting fibers (100μm core, High OH, NA 0.22).The overall fiber bundle diameter is 2.1 mm. On the proximal end, the collecting fibers are arranged in a vertical line in order to optimize light coupling with a monochromator Oriel Cornerstone 260 (Newport, Irvine, CA, US). In order to avoid unwanted effects as stray-light, a F$\sharp$ matcher (Newport, Irvine, CA, US) is placed in front of the monochromator input slit. A high sensitivity PMT H7422 (Hamamatsu, Hamamatsu City, Japan) is placed at the output slit of the Monochromator.

3.2.2 Fluorescence spectroscopy

Fluorescence spectroscopy acquisitions are accomplished by using a custom-made software developed in Labview ambient. Analog and Digital I/O are controlled by means of a NI 6221 DAQ board (National Instruments, Austin, TX, US). The output signal from the PMT is first sent to a preamplifier stage C6438-01 (Hamamatsu, Hamamatsu City, Japan) and then read on an analog input channel of the I/O board. The Labview program allows to change: the grating, according to the spectral region to be investigated, the starting wavelength, the ending wavelength, the scanning step and the acquisition time. For each spectral point the signal out from the preamplifier is read and saved together with the corresponding wavelength in a text file.

3.2 Multi dimensional-purpose fiber probe

The spectral resolution depends on the dimensions of the input/output slits aperture and on the grating used. Using a remote-controlled filter wheel it is possible to change the bandpass filter placed in front of the detector in order to block the excitation laser line. The filters used are two longpass, one at 400 nm (Melles Griot, Albuquerque, NM, US) and the other at 457 nm (LP02-458RS-25, Semrock, Rochester, NY, US) cut-off wavelength.

A first test measurement was accomplished on fluorescein, a well-known fluorophore. The measured fluorescein emission spectrum, together with the theoretical spectrum are represented in Fig.3.10. The small disagreement between the two spectra is due to the instrument spectral response R. In fact, the collected signal S is the convolution between the emitted fluorescence F and the instrument response R, which is in general dependent on the response of all the components, including the transmission of the multimode (MM) fibers, the reflectance of the mirrors and of the grating and the spectral sensitivity of the PMT.
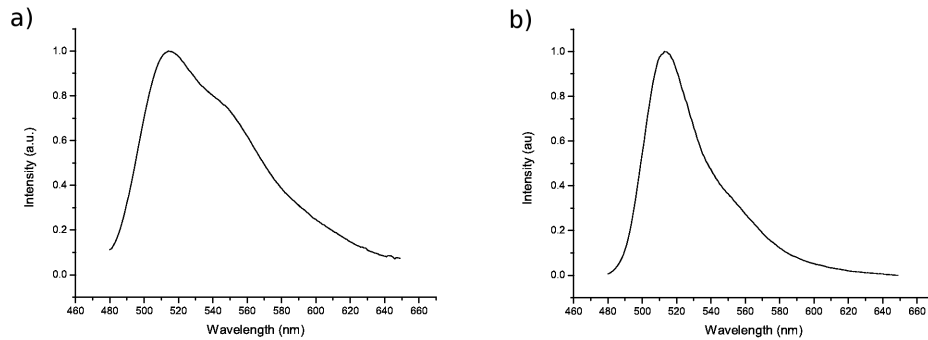

Figure 3.10: Fluorescence emission spectrum of fluorescein recorded by the fiber probe a) and theoretical b). Excitation wavelength: 445 nm. Resolution: 1 nm.

Furthermore, we performed a first *in vivo* test on human skin The spectra acquired at 378 nm and 445 nm excitation wavelength are shown in Fig.3.11. In both cases we used a 600 lines per mm grating, a monochromator slits aper-

ture of 150 μm, yielding a spectral resolution of 1 nm. The acquisition time was 10 s, and it was limited by the scanning speed of the monochromator.
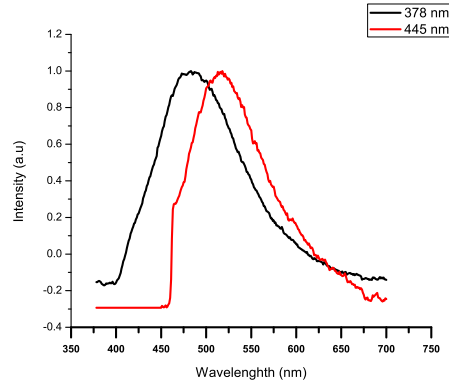

Figure 3.11: Normalized *in vivo* fluorescence spectra of human skin at 378 nm (black) and 445 nm (red) excitation wavelength. The step on the 445 nm excitation wavelength at 457 nm is due to the cut-off of the bandpass filter. Spectral resolution: 1 nm. Acquisition time: 10 s.

A more accurate calibration of the set-up could be performed by using a calibrating light source. By acquiring the spectrum of the calibration source is then possible to extract the system response by deconvolving the spectra acquired with the spectrum of the calibrating light source given in the data sheet.

3.2.3 Fluorescence lifetime measurement

Fluorescence lifetime measurement is accomplished by digital frequency domain FLIM (DFD-FLIM), using the ISS Fast-Flim board (ISS, Champaign, Illinois, US). According to literature [56] this method shows similar precision and accuracy with respect to TCSPC. The choice of this technique is due to the fact that it uses digital modulated laser sources with higher output power than picosecond pulsed diode laser required for TCSPC. Furthermore, the main electronics core in DFD-FLIM is a FPGA chip (cost around 100$)

that makes this technique really cheaper with respect to TCSPC. In comparison with normal frequency domain methods, since the heterodyning occur digitally, DFD-FLIM does not require radio frequency (RF) gain modulated detectors and RF amplifier electronics. Hence, DFD-FLIM works at full detector efficiency, improving the duty-cycle up to 100%. Moreover, by decomposing the digtal excitation pulses used in DFD-FLIM and the emitted fluorescence signal in their Fourier components, it is possible to acquire simultaneously two or more harmonics and therefore resolving two or more decay components.
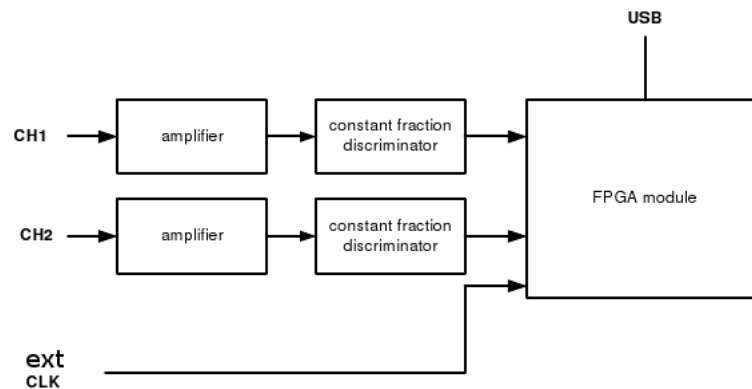
Fast-FLIM board

Figure 3.12: Block-diagram of the Fast-FLIM board. The board has two input channels. The signal out from the PMT is first pre-amplified and then sent to a CFD. The digital pulses out from the CFD are fed to the FPGA module. An external trigger provide the synchronization with the laser digital modulation.

In Fig.3.12 a block-diagram of the Fast-FLIM board is presented. The board has 2 different input channels for being used with two PMTs. A preamplifier stage, followed by a constant fraction discriminator (CFD), is mounted on each channel. The signal out from the CFD is fed into the FPGA module. The Fast-FLIM accepts an external trigger for synchronization with the laser

source modulation or it can provide itself a reference signal, depending on the firmware loaded in the FPGA module. In our case we use a custom-made electronic board that provides both the digital modulated signal for the lasers and the synchronization signal. Laser sources can be modulated digitally at 20, 30 or 40 MHz with 5 ns digital pulses. The choice of the modulation frequencies depends on the expected lifetime we want to measure.

Lifetime calibration

In the frequency domain, lifetime measurements are performed by measuring both the phase shift between the excitation and the fluorescence signal and the modulation amplitude. Since the phase of the excitation source is unknown, a calibration is required before performing the measurement. Lifetime calibration and acquisition are performed by using VistaVision, a software supplied by ISS. After having set the grating, the wavelength and the bandpass filter, we calibrated the Fast-FLIM board by measuring a known lifetime provided by a fluorescence standard solution. In our case we used Coumarin6 (Coumarin6, Sigma Aldrich, St. Louis, MO, US) that has a fluorescence lifetime of 2.5 ns. A list of fluorescence standards can be found in the ISS homesite (http://www.iss.com). The calibration provides a reference value for both phase shift and modulation amplitude. Those values will be used as a reference to calculate the lifetime of the sample under investigation. The excitation laser had a 5 ns digital pulse and a repetition rate of 30 MHz. Acquisition time was 10 s. The fit on the acquired data was done by using ISS Vinci software. An example of the plot of phase shift and modulation amplitude plots with corresponding fits is shown in Fig.3.13. The corresponding fluorescence exponential decay is shown in Fig.3.14 . The ISS Vinci program allows to set the number of harmonics to be used in the fitting routine. The lifetime distribution can be Lorentzian, Gaussian or discrete. The choice of an *a priori* distribution is due to the fact that ISS Vinci program performs the fit on the whole set of acquired data.
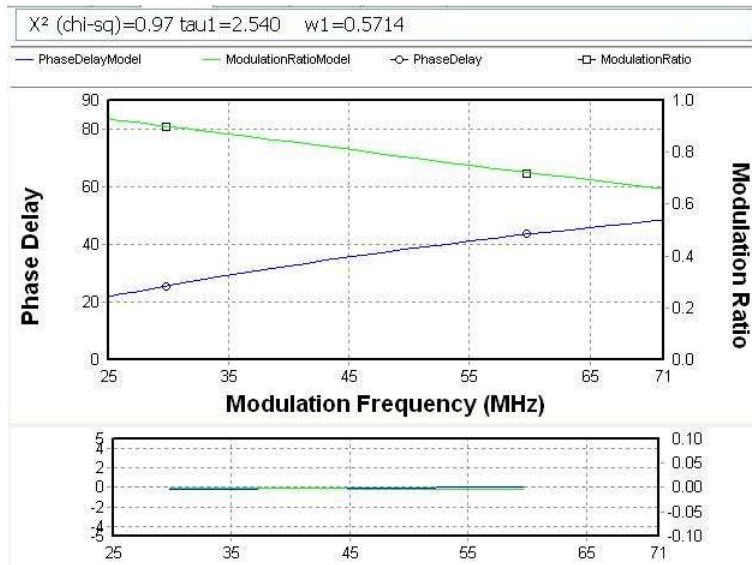
Figure 3.13: Plot of the phase shift (circle) and modulation amplitude (squared) values of Coumarin6 fluorescence, measured at 30 MHz (1st harmonic) and 60 MHz (2nd harmonic). Laser excitation wavelength: 445 nm. Digital pulses: 5 ns. Repetition rate: 30 MHz. Detection wavelength: 500 nm. Lifetime measured was 2.5 $\pm$ 0.5 ns. Corresponding fit on phase shift (blue) and modulation amplitude (green) of Coumarin6 fluorescence. Normalized χ^2=0.97.
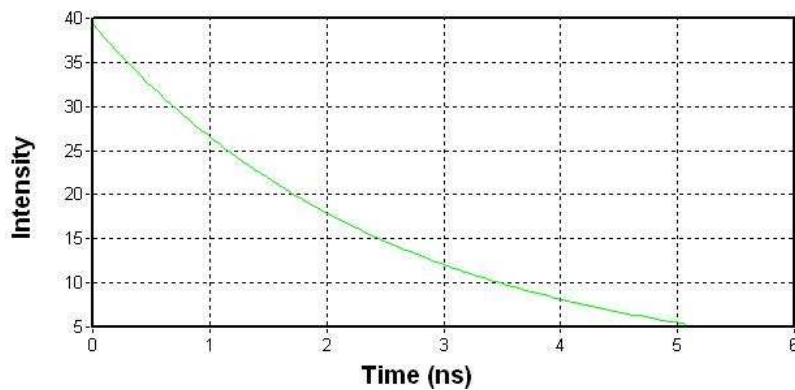

Figure 3.14: Lifetime fluorescence decay of Coumarin6 corresponding to the measurement shown in Fig.3.13.

In the measurement shown we used the first two harmonics, 30 MHz and 60 MHz, and a Gaussian distribution. We considered the FWHM of the

distribution as error in the measurement. A plot of the lifetime distribution is shown in Fig.3.15 .
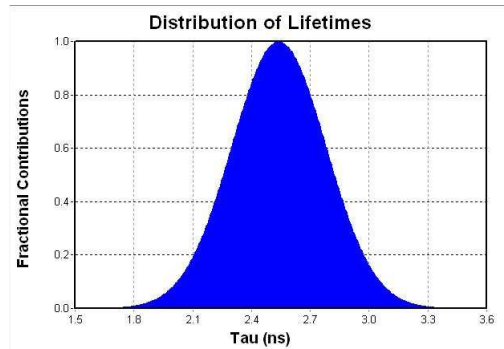

Figure 3.15: Gaussian distribution of the fluorescence lifetime of Coumarin6.

3.2.4 Conclusion

In this section the multi-dimensional fiber probe was presented. The small size of the fiber bundle, 2.1 mm in diameter, and the possibility to sterilize it make the fiber probe a suitable tool for future multi-dimensional *in vivo* endoscopic application. The capability of the instrument was tested, giving encouraging results. Future works could be accomplished on both *ex vivo* and *in vivo* clinical applications on both animal and human model. Further improvements for faster time acquisition and increased spectral resolution will be performed by using a cooled CCD camera. Moreover the set-up is already equipped with a 785 nm diode laser for Raman spectroscopy, that will be performed with a dedicated custom-made fiber bundle[58].

Chapter 4

Time- and spectral-resolved two-photon imaging of healthy bladder mucosa and carcinoma in situ

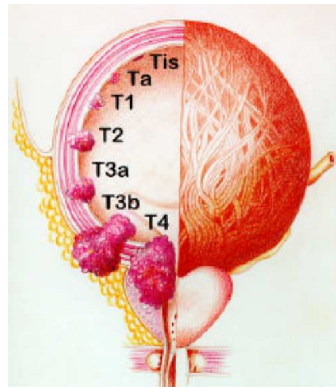Figure 4.1: Different grades of bladder tumor

During my PhD project I have made studies on multi-dimensional analysis on human tissues. Using a two-photon microscope, equipped with a FLIM set-up as described in the previous chapter, we were able to collect both chemical information, through fluorescence spectroscopy and lifetime imaging, and morphological information through microscopy. In this chap-

ter we present a study on human bladder fresh biopsies. In this study we examined both healthy mucosa and carcinoma *in situ*, showing that spectroscopic information, as the Red-Ox ratio, are important for early cancer diagnosis. The evaluation of nuclear to cytoplasm dimension ratio is another discrimination parameter coding for malignancy.

4.1 Bladder carcinoma *in situ*

Bladder cancer is one of the most common cancer in Western World[59]. Urothelial cell carcinoma represents from 90% to 95% of all bladder cancers. Carcinoma *in situ* shows a high risk of invasive progression and recurrence rate up to 85%[60]. Therefore an early detection and treatment are crucial for its curability. Even if the golden standard for cancer detection is biopsy followed by histology, this technique is invasive and requires several days to have a response. In the past decades clinical diagnosis was accomplished by white light (WL) cystoscopy, an endoscopic technique for urinary bladder. The cystoscope is basically a telescope mounted in a rigid tube. By using an optical fiber the image is carried from the tip of the cystoscope to a monitor. Suspicious areas are excised by the doctor, using endoscopic scissors, and then undergo histopathologic analysis. Unfortunately WL cystoscopy does not have enough sensitivity to detect all the tumoral lesions [61]. In the last years, with the development of fluorescence cystoscopy based on aminolevulinic acid (5-ALA) [62, 63], the sensitivity was increased up to almost 100% [62, 63, 64]. ALA is a naturally occurring, 5-carbon, straight-chain amino acid. ALA is expressed inside mithocondrial membrane by ALA-S enzyme, along its metabolic pathway it is transformed first in protoporphyrin IX (PpIX)[65] then, by attaching an iron atom in its ferrous (Fe2+) state, it becomes haem. ALA expression in cells is usually modulated by a negative feedback in the system, accomplished by haem. By artificially introducing ALA into the tissue the negative feedback is bypassed. Since in some pre-malignant and malignant lesions the enzyme responsible for the protoporphyrin IX catalysis has an increased activity, in those lesions an accumulation of PpIX is expected. In fluorescence cystoscopy blue-violet

light is used to detect fluorescence of porphyrins accumulated in the tumoral and inflammatory lesions. Even if fluorescence cystoscopy has many benefits as reduction of recurrance due to more complete resection[66, 67], it presents a high percentage of false positive, up to 39% [68, 69]. One big step beyond was made this year by the development of high magnification cystoscopy, with which is possible to increase the specificity up to 85% [70].
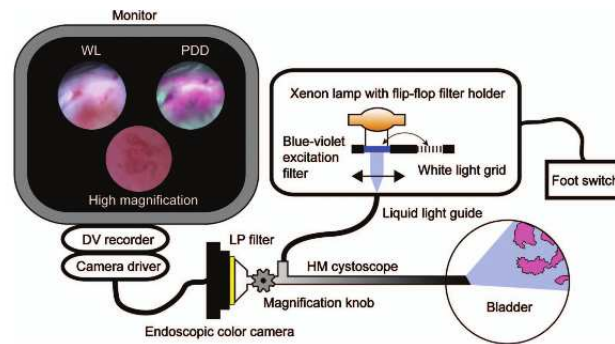

Figure 4.2: Working principle of high magnification fluorescence cystoscope. Suspected lesion found by fluorescence cystoscopy can be magnified. From vascular pattern analysis false positive tissues can be rejected up to 85% specificity[70].

4.2 Optical Biopsies of bladder mucosa

The aim of our research was to develop a new method for analysis and diagnosis of bladder cancer. This method is intended to be a self-standing or to be used beside fluorescence cystoscopy in order to reduce the amount of false positives. By using our multi-photon microscope described in the previous chapter we analyzed tissue samples of healthy bladder mucosa and carcinoma *in situ* (CIS). The microscope gave us important information on the morphology, and by proper filtering, on SHG contribution. Through the FLIM set-up we investigated the fluorescence emission spectra and fluorescence lifetime.

Non linear microscopy is widely used in order to achieve "optical biopsies" of biological tissues. Morphological signature of skin tumoral cells through TPE fluorescence was already demonstrated [38]. The diagnosis relies on the ratio between the whole area of a cell and the area of its nucleus. In TPE microscopy the measurement could be easily done since fluorescence signal arises only from cytoplasm while the nucleus does not give any contribution. Two-photon imaging microscopy was already used on bladder cell cultures [71] as well as on bladder tissue samples from animals [72, 73], but a test on the capabilities of multi-photon microscopy in detecting human bladder cancer have not been reported so far.

A further increase in specificity can be obtained by using fluorescence spectroscopy [74]. A measurement of the Warburg effect [39] can be done by calculating the ratio between FAD and NADH contributions in fluorescence signal when exciting at two proper wavelengths, as 740 nm and 890 nm. Moreover, information on epithelial cell growth can be derived from the SHG signal coming out from the specimen.

Lifetime imaging is an additional method used. By fitting the exponential fluorescence decay with a double-exponential decay function it is possible to extract a fast and a slow component that can be related to the free or protein bound state of a particular molecule, as such NADH and FAD.

4.3 Material and methods

4.3.1 Bladder fresh biopsies

On five patients with positive urine cytology two sets of of cold-cup bladder biopsies were taken. Using white light cystoscopy healthy and suspected CIS samples were identified and excised during transurethral resection of bladder. One set was used for histology that confirmed CIS in all suspected samples. The other set was stored in a wet environment with few drops of physiologic saline solution and used within one hour for two-photon imaging.

4.3.2   Image acquisition

Fresh tissue biopsies were placed between a slide and a 170 μm thick coverslip. In order to prevent unwanted movements of the sample a fat silicon ring was placed around it. The sample was immersed in few droplets of PBS with the purpose of maintaining its natural osmolarity. All images were acquired using "en-face" optical sectioning geometry (optical axis perpendicular to the tissue surface).

For each sample we acquired three TPEF images 100μm x 100μm field of view, 1024x1024 pixels resolution, exciting at 740 nm; and one SHG image exciting at 840 nm. The laser power at the sample surface had a mean value between 10 mW and 40 mW, depending on the depth of recording, and the pixel dwell time was 5 μs. For spectral and lifetime measurements we acquired three single-channel FLIM images with 100μm x 100μm field of view, 128 x 128 pixels resolution, and three 16-channels images 20μm x 20μm field of view, 32x32 pixels resolution. Laser mean power was 15 mW and the acquisition time was 40 s for single-channel and 160 s for 16-channels acquisitions.

4.4   Results and discussion

4.4.1   Morphological analysis (TPEF and SHG)

When exciting at 740 nm the main fluorescence contribution arises from NADH, which is still present in fresh biopsies [44, 74] up to 4-5 hours from excision. The SHG signal observed, when exciting at 840 nm, originates mainly from the collagen fibrils located in the connective tissue. Both SHG and TPEF allow sub-diffraction limited spatial resolution. Moreover in both healthy mucosa (HM) and CIS samples cells emit a high fluorescence signal since the tissue was excised and analyzed within 2-3 hours. Hence, we were able to image the urothelium with a resolution up to sub-cellular level. Acquired TPEF and SHG images were merged in RGB images and visualized using ImageJ (NIH, Bethesda, Maryland USA). In order to remove the background and to enhance both cellular and nuclear borders, a threshold was

applied to the images. The color code used was green for TPEF and blue for SHG. The merged images are in good agreement with the corresponding histological images taken from the same sample, as shown in Fig.4.3.
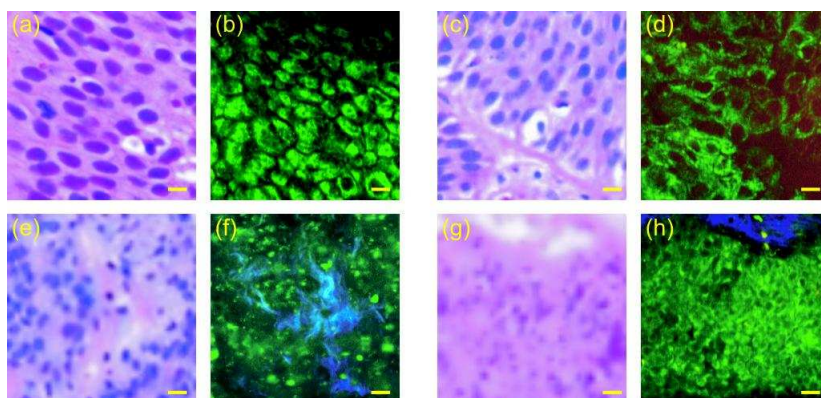

Figure 4.3: Histological images of human bladder biopsies taken after H&E staining and the corresponding TPEF-SHG images. The color code used is green for TPEF and blue for SHG. Scale bar: 10 μm. Healthy urothelium histology (a) and the corresponding TPEF image (b). Carcinoma *in situ* proliferation histology (c) and the corresponding TPEF image (d). Histological image of healthy mucosa (HM) with underlying collagen (e) and the corresponding TPEF-SHG image (f). Histological image of CIS-connective tissue border (g) and the corresponding TPEF-SHG image (h).

The most interesting result coming out from morphological analysis is the cellular to nuclear dimension ratio. As we asserted in the previous paragraph, fluorescence signal arises only from cellular cytoplasm, whilst the nucleus does not give any contribution. In the acquired images is clearly visible that the nuclear dimension is larger in CIS cells. In order to give a more accurate quantitative measurement of this effect, 10 cells per image were chosen and their cellular and nuclear area were evaluated in squared pixels, as shown in Fig.4.5. The results of cellular to nuclear dimension ratio for both HM and CIS are shown in the bar histogram plotted in Fig.4.4. CIS has in average a lower ratio in comparison with HM. This morphological signature of cancer was already demonstrated by TPEF microscopy in other tissues, as skin [38].

Anyway, in order to confirm this promising result, a larger data set would be suitable. Furthermore, the analysis can be improved by a dedicated program for automated cell recognition, even if a very high image contrast is required.
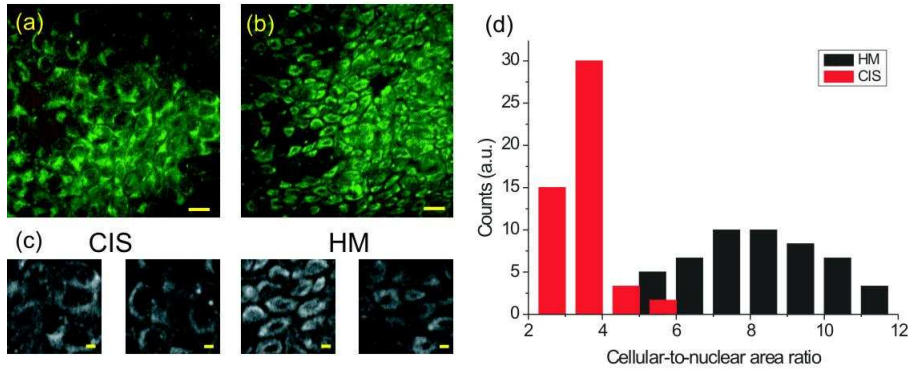
Figure 4.4: TPEF image of cellular proliferation in CIS (a) and in HM (b). Scale bar: 10 μm. Magnified examples of ROIs (c) used for the cellular to nuclear ratio calculation. Scale bar: 3 μm. Bar histogram of the cellular to nuclear ratio distribution (d), in red for CIS and in black for HM.
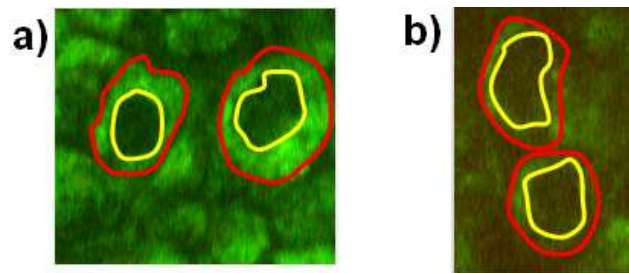
Figure 4.5: Example of cellular (red) to nuclear (yellow) dimension ratio for HM (a) and CIS (b)

4.4.2   Tissue spectral features

Multi-spectral two-photon imaging (MTPE) was performed by using the photon counting detection set-up. For each sample we took a set of MTPE images, 20μm x 20μm field of view, 32x32 pixels resolution, exciting at 740 nm

and 890 nm. Images were taken in a depth range of 50-60 μm. The emission
spectra in the range 420 nm - 620 nm were acquired using the 16-channels
PMT array with a resolution of 13 nm. We obtained then, for each mea-
surement, a set of 16 images 32x32 pixels in which each image corresponds
to a particular fluorescence channel. The sum of the intensity values of the
image pixels yields to an evaluation of the intensity detected in the corre-
sponding spectral channel. The fluorescence spectra at 740 nm and 890 nm
excitation wavelength, averaged on 5 images of both CIS and HM are shown
in Fig.4.6a and in Fig.4.6b, respectively. It is clearly visibile that spectra are
quite similar: they are superimposable at 740 nm excitation and they show
just a difference around 445 nm at 890 nm excitation, indicating the pres-
ence of the SHG signal. We validated this assumption by performing lifetime
analysis (data not shown). In fact we verified that the main contribution of
the signal at 445 nm arises from photons detected at time delay zero with
respect to excitatin pulse, hence from scattered photons.

In order to give a more quantitative evaluation of the SHG contribution, we
used as a score the SHG-to-autofluorescence ageing index of dermis (SAAID
[75]), defined as

$$SAAID = \frac{SHG - TPEF}{SHG + TPEF} \qquad (4.1)$$

where SHG and TPEF are the second-harmonic and autofluorescence signal
intensities, respectively. We considered as SHG the signal made by the sum
on the detector channels in the 420 nm - 475 nm range, while autofluores-
cence is given by the sum of the detector channels in the 475 nm - 620 nm
range.

The distributions of the values of SAAID for HM and CIS are represented
in Fig.4.6d. False color SAAID maps for HM and CIS are shown in Fig.4.6c.
The poor spatial resolution is due to the necessity to increase the number of
temporal and spectral channels, paid in term of a reduced spatial resolution.
In case of CIS the distribution is shifted towards negative values, indicating a
prevalence of signal arising from TPEF and a low contribution of SHG. This
is probably related to the higher cellular proliferation in tumoral tissues with
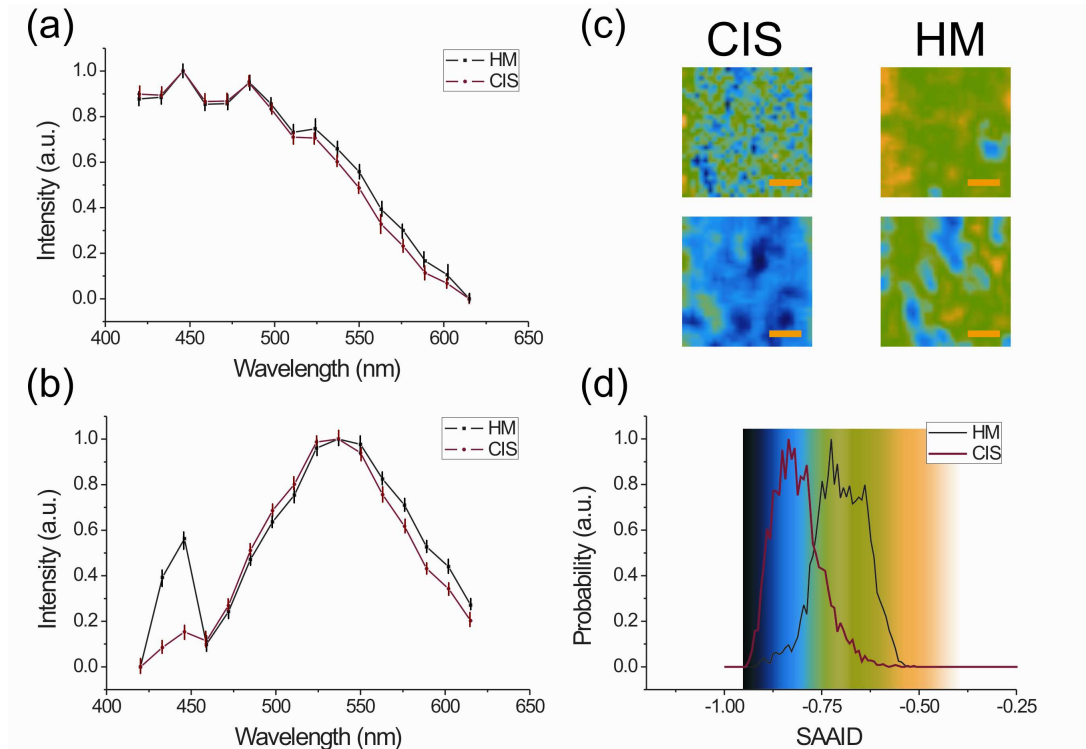
Figure 4.6: TPEF spectra of HM (black) and CIS (red), measured by summing the detected photon number over a region of 20 μm x 20 μm at a depth of 50-60 μm, and by averaging on 5 samples of CIS and 5 samples of HM; exciting at 740 nm (a) and 890 nm (b). Two examples of SAAID maps (c), calculated using Eq.4.1 and using false color as in SAAID distribution (d) of CIS (red) and HM (black). Scale bars: 5 μm.

respect to healthy tissues. Anyway, since cellular proliferation in CIS occurs mainly in the superficial layer in the first stage, this datum does not seem to be a strong feature for tissue discrimination. In any case SHG microscopy can yield to important information in studies on the relationship between cancer growth and collagen disruption [76].

An important feature for cancer discrimination arises from spectral analysis of NADH/FAD fluorescence contribution. Healthy and tumoral cells use two different metabolic pathways for energy production. According to the Warburg effect [39], ATP production in tumoral cells is mainly due to glycolysis biochemical pathway in comparison with healthy cells in which phosphory-

lation dominates. In Fig.4.7a and Fig.4.7b the two metabolic pathways are
shown. In the case of phosphorylation both NADH and FAD are involved as
electron carriers, whereas in the case of glycolysis only NADH is involved.
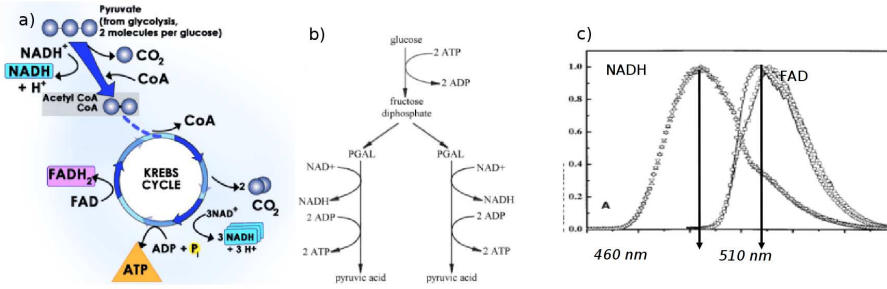
Figure 4.7: Biochemical pathways for phosphorylation (a) and for glycolysis
(b). Fluorescence emission spectra of NADH and FAD (c)

The fluorescence emission spectra of NADH and FAD are represented in
Fig.4.7c. In our analysis we assume that the NADH content inside the sam-
ple is proportional to the emitted fluorescence in the range 459 nm - 472
nm, when exciting at 740 nm. In addition, the FAD content should be pro-
portional to the emitted fluorescence in the range 511 nm - 524 nm, when
exciting at 890 nm. After proper correction of the signals, taking into ac-
count the detector spectral response and the square of the excitation power
at the objective aperture, we introduced the Red-Ox score, defined as:

$$RedOx = \frac{FAD - NADH}{FAD + NADH} \tag{4.2}$$

Images of HM, excited at 740 nm and detected in the 459 nm - 472 nm range
as well as excited at 890 nm and detected in the 511 nm - 524 nm range are
shown in Fig.4.8a and Fig.4.8b, respectively. The poor spatial resolution is
still due to the necessity to increase the number of temporal and spectral
channels, paid in term of a reduced spatial resolution. The Red-Ox maps
for HM and CIS are represented in false color in Fig.4.8c, together with the
corresponding images (Fig.4.8c).

Figure 4.8: MTPE images of HM acquired: at 740 nm excitation wavelength and detected in the 459 nm - 472 nm spectral range (a); at 890 nm excitation wavelength and dete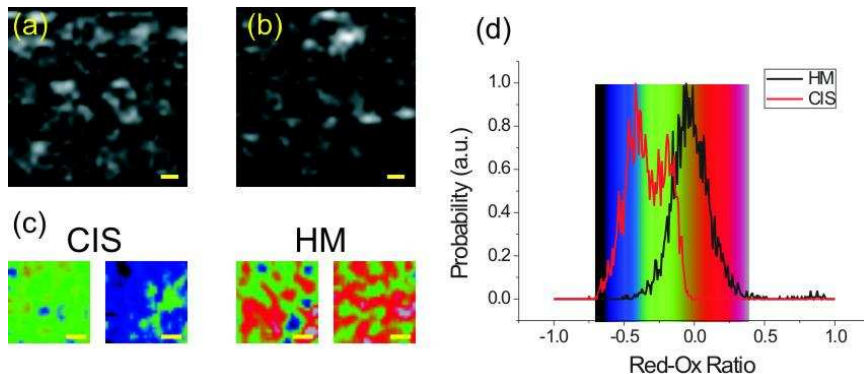cted in the 511 nm - 524 nm spectral range (b). Scale bars: 2 μm. Two examples of Red-Ox maps (c) for both HM and CIS, calculated using Eq.4.2. The color-coded scale arise from the RedOx distribution (d) for HM (black) and CIS (red). The distribution is obtained by averaging on 5 samples of both CIS and HM.

From the Red-Ox distribution in Fig.4.8d we can observe a lower oxidative stress in normal tissue with respect to cancer, as expected. In other words, in CIS there is an unbalance between NADH and FAD with respect to HM, probably caused by a higher production of energy from glycolysis, where just NADH is involved.

4.4.3 Fluorescence lifetime of NADH-FAD couple (FLIM)

Another way to characterize NADH and FAD emission is represent by lifetime analysis. Both NADH and FAD have different fluorescence lifetimes depending if they are in their free or protein-bound state. NADH has a typical fluorescence lifetime of 0.3 ns when it is free, while when it is protein-bound the lifetime has a value around 2 ns, depending on the molecule to which it binds. FAD instead has a free lifetime of 2 ns and a lifetime of less than 1 ns when it is protein bound. Therefore, by fitting the measured decay traces using a double-exponential decay function, it is possible to obtain a fast and a slow lifetime component that can be related to the free and protein-bound

state of the molecule examined. This approach was already used in both cell cultures [71] and fresh punch biopsies from animals [72, 73]. We performed lifetime analysis of NADH, using 740 nm excitation wavelength and detecting in the 459 nm - 472 nm range, and of FAD, using 890 nm excitation wavelength and detecting in the 511 nm - 524 nm range. TPEF images of HM and CIS are displayed in Fig.4.9a and in Fig.4.9c, respectively. The lifetime measurement was done through TCSPC technique. Using SPC-Image 2.8 we first de-convolved the instrument response function from the decay trace and then we fitted the fluorescence decay profile with a double-exponential decay function, as follows:

$$F(t) = a_1 e^{-t/\tau_{fast}} + a_2 e^{-t/\tau_{slow}} \qquad (4.3)$$

with the normalization condition

$$a_1 + a_2 = 1 \qquad (4.4)$$

Then, by looking at the a_1/a_2 parameter we obtain a quantitative score for the ratio between free and protein-bound NADH, and *viceversa* for FAD.

The distributions of a_1/a_2 for NADH and FAD, for both HM and CIS, are shown in Fig.4.9e and Fig.4.9f. Corresponding false color images are displayed in Fig.4.9b for HM, and in Fig.4.9d for CIS. Even if oxidation and tissue degradation should start immediately after excision, we did not observe any relevant fluctuation of lifetime in a period of 2-3 hours. In order to validate the hypothesis of a double-exponential decay, we performed a fit on the acquired traces using both single- and double-exponential decay functions. The corresponding normalized χ^2 distributions are shown in Fig.4.10. In case of double-exponential decay the χ^2 distribution is centered around one, confirming a better agreement with the experimental data in comparison to the single-exponential decay.
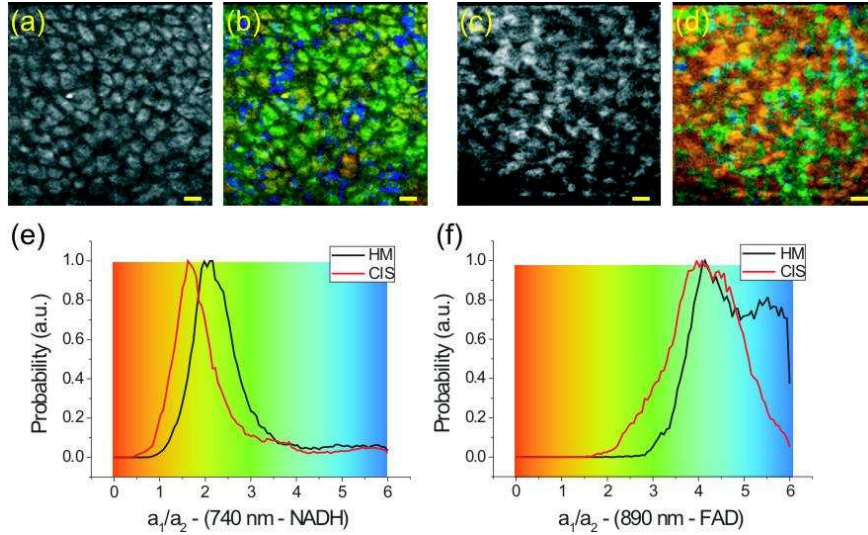
Figure 4.9: TPEF image of HM (a) and CIS (c). Excitation wavelength: 740 nm and detection wavelength range: 459 nm - 472 nm. Field of view: 100 μm x 100 μm. Depth: 20 - 30 μm. Corresponding color-coded images of a_1/a_2 distribution for HM (b) and CIS (d). Distributions of a_1/a_2 for HM (black) and CIS (red), exciting at 740 nm and detecting in the 459 nm - 472 nm range (e), exciting at 890 nm and detecting in the 511 nm - 524 nm range (f). Distributions are obtained by averaging on 5 samples of CIS and 5 samples of HM.
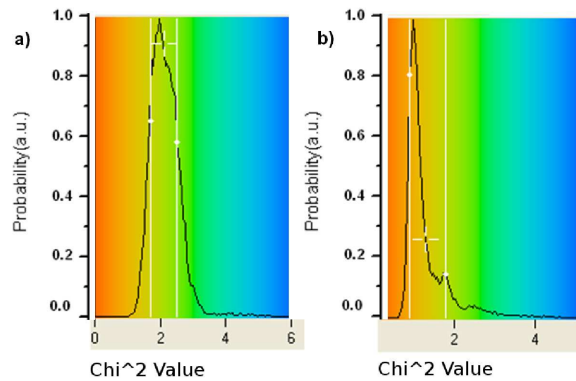
Figure 4.10: Comparison between the normalized χ^2 distribution in case of single-exponential decay (a) and in case of double-exponential decay (b). The latter is centered around one, validating the hypothesis of double-exponential decay.

As expected in case of NADH, the a_1/a_2 distribution has lower values for CIS, indicating a higher contribution from the slow component, therefore from protein-bound NADH. In case of FAD a higher values of a_1/a_2 in healthy tissues could be related to the domination of phosphorylation, where FAD is present in a bound state. Finally we can claim that lifetime measurements can be a powerful tool to optically record the Red-Ox state of a tissue, therefore for to be used in early diagnosis of cancerous and precancerous conditions, as in the follow-up of cancer-targeted therapies. Further improvements and validations could arise from *in vivo* measurements.

4.5   Conclusion

In this chapter we introduced the problem of early diagnosis of bladder cancer and its state of the art. We proposed an alternative diagnostic method in order to increase specificity. The capability of multidimensional analysis was successfully demonstrated both for morphological and spectroscopic analysis. In particular, we found morphological differences between HM and CIS, measured in terms of nuclear to cellular dimension ratio, as well as spectroscopic differences, measured in terms of SAAID score, Red-Ox score and lifetime analysis. The obtained results were published on an international peer-reviewed journal [77]. Improvements of our research should involve a higher amount of samples in order to have a statistically significant confirmation of our promising method. Future analysis should also include inflammatory tissue and tumoral tissues with different grades. A proper algorithm for automated cell recognition may be helpful for increasing the statistics. Test of this method *in vivo* could give rise to important improvements in both diagnostic sensitivity and specificity. Finally this method may be tested on other pathologies and its *in vivo* application could represent a new powerful tool for tissue discrimination and diagnosis.

Chapter 5

Scoring of collagen organization in human dermis by two-photon microscopy

The subject of this chapter is the characterization of collagen pattern in of healthy dermis, normal scars and keloids, by TPEF-SHG imaging. In the study on bladder tissue, presented in the previous chapter, we emphasized the important role of tissue fluorescence and spectroscopy for discriminating cancer from healthy tissue. On the opposite, in the study described here, we focus mainly on the morphological information provided by two-photon fluorescence and second-harmonic generation microscopy.

Autofluorescence of endogenous molecules as NADH, FAD, keratins, melanin, cholecalciferol and others allows imaging of skin without employment of any exogenous fluorophore [78, 44]. TPEF microscopy on skin is a well-established technique and it has been already widely used in *ex vivo* and *in vivo* on both animal and human model [16, 79]. TPEF can provide "optical biopsies" of a tissue by means of morphological characterization [80, 79, 81, 82]. Beside TPEF, SHG microscopy is another important tool for imaging connective tissues such as cutaneous dermis [83, 28]. SHG was already demonstrated to be an extremely powerful tool for studying the organization of non-centrosymmetric molecules as collagen [84, 29], which is

the most important component of connective tissues. Recent studies have
shown its capability in the investigation of structural changes in fibrotic col-
lagen [27], human dermis [28, 29], keloids [30], cornea [31, 32] and tumor
microenvironment [33]. The combination of TPEF and SHG is particularly
powerful when imaging dermis because the two main components of dermis,
elastin and collagen, can be respectively imaged by TPEF and SHG without
any staining. Several studies involving combined TPEF-SHG were conducted
on skin physiology and pathology as cutaneus photoaging [75, 85], psoriasis
[16] and skin tumor, including basal cell carcinoma (BCC) [86, 87, 88] and
malignant melanoma (MM) [38, 18, 89].

5.1   Collagen patterns in healthy dermis, nor-
mal scars and keloids
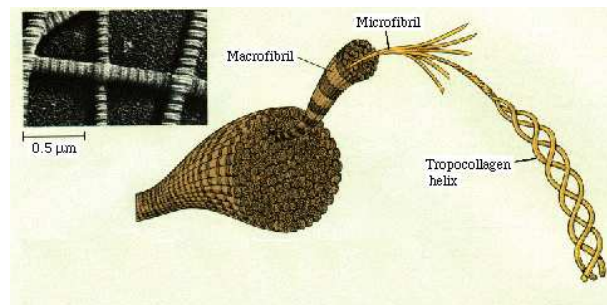
Figure 5.1: Collagen structure, collagen fibers are composed by collagen fib-
rils bundle together. Fibrils are in turn composed by an assembling of a thin
protein called tropocollagen. TEM image of a collagenous fiber (upper left)
[90].

In this study we tested and compared three different image pattern analysis
methods on SHG images of human dermis. In particular, we analyzed the dif-
ferences of collagen patterns of healthy dermis (HD), normal scars (NS) and
keloids (K) by means of three different scoring algorithms. The method pre-
sented, besides being an important tool for investigation of scar formation, is

5.1 Collagen patterns in healthy dermis, normal scars and keloids

potentially a suitable technique to follow-up skin treatments, including laser therapies.

We focused our analysis on collagen type I in skin dermis. Collagen is organized in fiber bundles with a typical diameter between 0.5 μm and 3 μm. Collagen fibers are made by a set of fibrils, the collagen molecular unit, tightly packed together side by side. Fibrils are in turn composed by an assembling of a thin protein called tropocollagen.

In HD collagen fiber bundles are interconnected by thin fibrillar strands and they are arranged in a parallel way to the epithelial surface. Both K and hypertrofic scars (HS) are characterized by excessive dermal fibrosis caused by an abnormal wound healing. In K fibroblasts have an intense proliferating activity, 20 times greater than in HD. Fiber produced are thick, randomly connected and the orientation is not necessarily parallel to the epithelial surface. K occurs in genetically susceptible people, mainly in darker-pigmented races and, in comparison with NS, they do not regress. Treatment of K is indeed not naive and an accurate follow-up must be done for each patient. Moreover in K the collagen synthesis overwhelm elastin, therefore we expected that the SHG-to-autofluorescence ageing index SAAID, introduced in the previous chapter, is a good candidate for tissue characterization. Difference in elastin distribution between HD and NS were also found [91]. In the first case elastin fibers have a homogeneus distribution inside collagen texture, besides in NS are tightly packed and well separated from collagen.

The collagen patterns of HD, NS and K are depicted in Fig.5.2 .Their differences can be easily distinguished by eye. A completely lack of elastin was found in K.

In order to analyze the differences in a more rigorous way we implemented two independent image pattern analysis methods. The first method uses the gray-level co-occurrence matrix (GLCM) of the SHG images. By calculating its correlation, homogeneity and energy it is possible to give an estimation of a typical length within which collagen maintains its organization. The second method exploits the spatial frequencies distribution of the intensity values of the SHG images, through analysis of the image in the Fourier domain. By analyzing the bidimensional intensity distribution of the FFT images we

can determine the level of organization of the collagen texture in terms of isotropy/anisotropy.
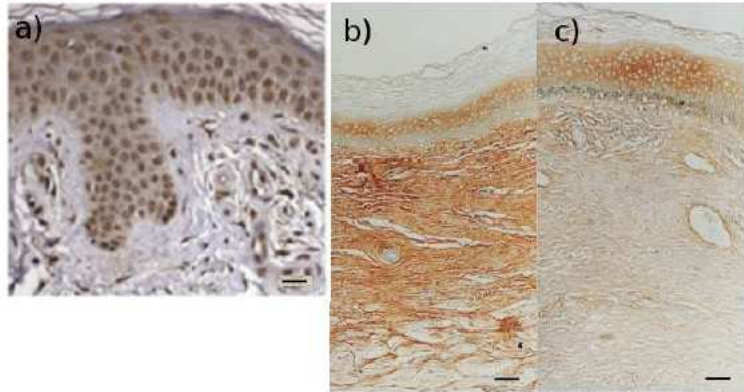
Figure 5.2: Histology images of Healthy Dermis (a), scale bar:400 μm. Normal Scar(b) and Keloid (c). Scale bar:200 μm [92].

5.2 Materials and methods

5.2.1 Samples

In this study we examined 3 samples of healthy dermis (HD), 2 of normal scar (NS) and 3 of keloids (K). NS and K samples were removed for esthetic reasons from five patients. HD samples were obtained out of discarded specimen after plastic surgery of the breast or abdomen. NS and K samples came with 2-3 mm of healthy skin margins. Parts of the samples were fixed with formalin and paraffin embedded for histopathology. The remaining parts were frozen, cut in slices, ranging from 50 μm up to 100 μm thickness, in a compact cryostat and imaged with two-photon microscopy. Before imaging samples were unfrozen and sandwiched between a microscope slide and a 170 μm thick coverslip. A droplet of PBS was added in order to maintain the natural tissue osmolarity.

5.2.2 Image acquisition

Images were acquired using the two-photon microscope described in chapter 3. The excitation wavelength used was 740 nm for TPEF and 840 nm for SHG. In the latter case a bandpass filter centered at 420 nm and with 20 nm bandwidth was employed in order to collect only signal arising from SHG. Mean laser power delivered to the samples was between 10 mW and 40 mW, depending on the depth of recording. In this power range photobleaching and photodamage are avoided. Acquired images have a spatial resolution of 512x512 or 1024x1024 pixels and a lateral dimension from 60 μm to 200 μm. With a pixel dwell time of 5 μs, the image acquisition time was 1.3 s for 512- and 5s for 1024- pixels images, respectively. Some FLIM images were acquired in order to confirm that the detected signal was SHG through a time-resolved analysis.

5.2.3 Image analysis

TPEF and SHG images were merged using ImageJ (NIH, Bethesda, Maryland USA). SAAID scoring was performed by a using a program developed in a Labview (National Instruments, Austin, TX, US) ambient. The values reported arise from a geometrical average of 10 ROI of 50 μm x 50 μm selected in each sample. A Matlab routine was employed for SHG image processing and GLCM analysis, according to [93, 94]. GLCM matrix and their correlation, energy and homogeneity were calculated running the neighbor index from 1 to 200. FFT intensity images were calculated using ImageJ and processed by a Matlab program. In order to emphasize statistical differences on SAAID and FFT anisotropy a *t-test* was realized using Microcal OriginPro8 software.

5.3 Results and discussion

5.3.1 Combined two-photon excited fluorescence (TPEF) and second-harmonic generation (SHG) imaging

Morphological investigation was accomplished through combined TPEF-SHG imaging. Examples of TPEF, SHG and merged images of samples of HD, NS and K are shown in Fig.5.3. TPEF is represented in the first column from the left, SHG in the second and their merging in the third .

As in the study on bladder tissue, presented in the previous chapter, we performed FLIM for confirming that the signal interpreted as SHG arises from scattering process and not from a fluorescence decay. In HD the arrangement of collagen fibers parallel to the epithelial surface is clearly visible, while K shows its characteristic thick fiber bundles. Moreover, in K sample it is also possible to discriminate different histopathologic features as fibroblastic/myofibroblastic cell proliferation (Fig.5.3g-fig5.3j) and amiantoid collagen fibers (fig.5.3j -fig.5.3l).

We characterized morphology through SAAID index in which the balance of collagen (emitting SHG) and elastin (emitting TPEF) is measured by the ratio

$$SAAID = \frac{SHG - TPEF}{SHG + TPEF} \tag{5.1}$$

The different values for HD, NS and K are shown in Fig.5.3m. We found a SAAID score negative in NS, due to a higher elastin content, while is slightly positive in HD and close to 1 in K, corresponding to an almost total absence of elastin. Statistical differences were highlighted at the 0.05 level by a statistical *t-test*.

5.3.2 GLCM analysis on HD and K

We analyzed the texture pattern using the GLCM method, with which it is possible to provide information on the relationship among pixels intensities value in an image. The method compares a pixel intensity value with the
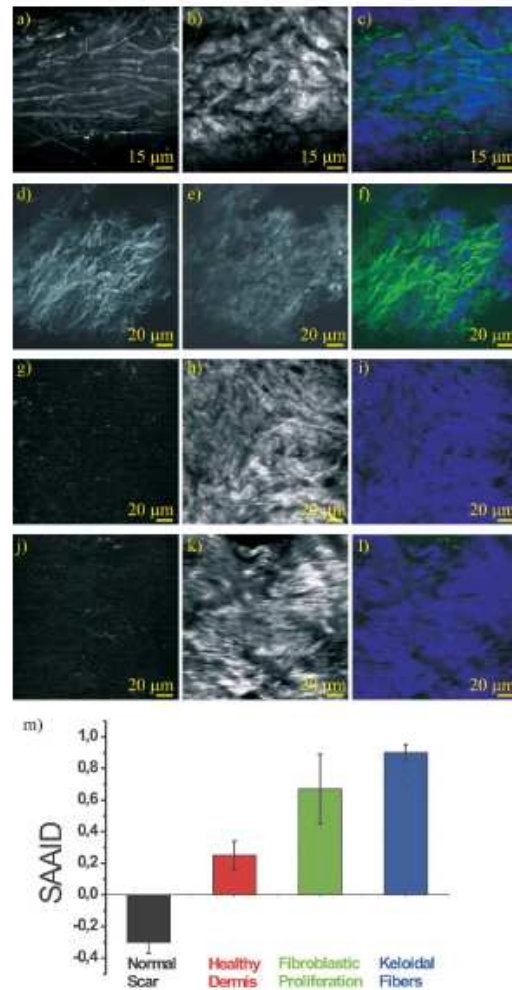
Figure 5.3: Transversal optical section (optical axis parallel to tissue surface) of *ex vivo* sample of healthy dermis (HD): TPEF (a), SHG (b), and the merge between the two images (c). Scale bar: 15 μm. Transversal optical section of *ex vivo* sample of normal scar (NS): TPEF (d), SHG (e), and the merge between the two images (f). Scale bar: 20 μm. Transversal optical section of *ex vivo* sample of keloid (K) with fibroblastic proliferation: TPEF (f), SHG (g), and the merge between the two images (h). Scale bar: 20 μm. Tranversal optical section of *ex vivo* sample of keloid (K) with keloidal fibers: TPEF (i), SHG (j), and the merge between the two images (k). Scale bar: 20 μm. Bar histogram of the SAAID index for HD, NS, fibroblastic proliferation and fibers in K.

intensities of the neighbors and it creates a matrix with a dimension related to the bit-depth of the image [93, 94]. An explanation of this methods can be found in Appendix A. Analysis on GLCM matrix can be done by calculating different parameters. These parameters are in general grouped in three classes: statistics, contrast, orderliness. In this analysis we selected one parameter per class. In particular we used correlation as statistical measurement, homogeneity as contrast measurement and energy as orderliness measurement. Correlation is a measure of dependence of two different pixel values and it was calculated from GLCM matrixes at different offsets. By looking at the behaviour of the correlation versus offset it is possible to extract useful information about the original image. If the image shows a certain recurrence in its structure it is reflected on a high correlation value at an offset corresponding to the recurrence length. Moreover, through correlation it is also possible to evaluate the distance between pixels within which the image can be considered correlated. By means of an exponential fit a decay length of correlation can provide indication on the sudden change of regularity of an ordered structure. Given a normalized GLCM matrix with elements $p_{i,j}$, the expectaction values μ_i and μ_j, the standard deviations σ_i and σ_j and correlation R are calculated as follows:

$$\mu_i \;=\; \sum_{i=1}^{N} i p_{i,j} \tag{5.2}$$

$$\mu_j \;=\; \sum_{j=1}^{N} j p_{i,j} \tag{5.3}$$

$$\sigma_i \;=\; \sqrt{\frac{1}{N-1}\mu_i} \tag{5.4}$$

$$\sigma_j \;=\; \sqrt{\frac{1}{N-1}\mu_j} \tag{5.5}$$

$$R \;=\; \sum_{i,j} \frac{(i-\mu_i)(j-\mu_j)p_{i,j}}{\sigma_i\sigma_j} \tag{5.6}$$

Our analysis also involved other two useful parameters as homogeneity and energy. The former is a weighted sum of the GLCM pixel values, in which

weights are non-linearly decreasing in value as the distance from the matrix diagonal increases. It is important to point out that in GLCM matrix the diagonal corresponds to all the neighbors pairs of pixels with the same value. So that, as the distance from the diagonal increases, as much the difference between neighbors intensities increases. Therefore homegeneity is related to the probability that a pixel and its neighbors have similar intensities. Besides, energy gives information on the hot spot of the GLCM matrix, hence it provides a measure of the orderliness. It is calculated by the root squared sum of the GLCM values. The expression for energy and homogeneity are the following:

$$H \quad = \quad \sum_{i,j} p_{i,j} \frac{1}{1 + (i+j)^2} \tag{5.7}$$

$$E \quad = \quad \sqrt{\sum_{i,j} p_{i,j}^2} \tag{5.8}$$

As previously described HD is characterized by collagen fiber arranged mainly parallel to the epithelial surface. According to literature fibers have a diameter ranging from 0.5 μm up to 3 μm [95]. Besides K is characterized by thicker bundles of collagen fibers randomly organized and more densely packed. Therefore we expect a longer correlation length and a higher value of homogeneity in K with respect to HD. The values of correlation, homogeneity and energy versus neighbor index (offset) are plotted in Fig.5.4. By fitting the correlation plot with a single exponential decay function it is possible to extract the decay length in both HD and K. The decay length we found are 3.7±0.1 μm and 6.8±0.1 μm for HD and K, respectively. Even if this values are not exactly the fiber bundle diameters, they are probably related to them. As supposed, K shows a longer decay length than HD. Regarding energy (5.4c) and homogeneity (5.4b) K has higher values than HD. Indeed K is expected to be more uniform than HD. The similar results in energy and homogeneity arises from the fact that they are not independent each other. In conclusion we demonstrated that GLCM analysis is a powerful tool to characterize organization of fibrillar collagen in SHG images.
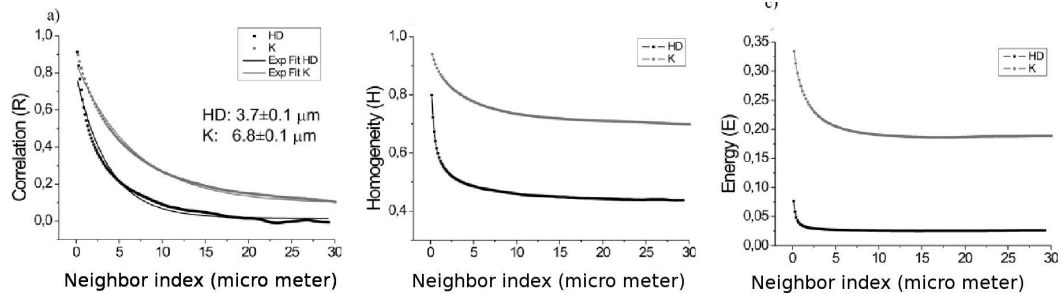
Figure 5.4: Plot of Correlation (R), Homogeneity (H) and Energy (E) versus neighbor index of HD (black squares) and K (grey circles). In the Correlation graph the fit with a single exponential decay is superimposed (black line).

5.3.3 FFT analysis on HD and K

The spatial information embedded in SHG images of collagen fibers can be transformed into frequency components by using Fast Fourier Transform (FFT). If in the original SHG image the pattern shows a particular periodicity or arrangement it will be highlighted in the Fourier space. Therefore FFT could be suitable for assigning a degree of organization. In the images of fibrillar collagen FFT analysis is especially helpful for characterizing the degree of symmetry. In fact, let's suppose to have an image of aligned fibers. On the corresponding FFT image we expect higher values on the direction perpendicular to the direction of the fibers, and lower values in the parallel one. The resulting FFT distribution plot is therefore elliptical with major axis on a direction perpendicular to the direction of the fibers. On the opposite, if we have an image of misaligned fibers, randomly connected and arranged, we expect a circular distribution plot in the Fourier space. Hence, a measure of the anisotropy of the image can be given by simply calculating the ratio of the axes of the ellipse in the FFT image. This ratio will range from 0 (maximum anisotropy) to 1 (perfect isotropy).

In order to evaluate the aspect ratio (AR) of the distribution, we caluclated

the covariance matrix between rows and columns of the plot. Finally by calculating eigenvectors and eigenvalues of the matrix, we evaluated the AR by the sqaure root of the ratio between the two eigenvalues. The effective result of this operation is a rotation of the (x,y) axis in new directions in which along one axis the variance has the maximum value and along the other has the minimum one. Therefore, since the two eigenvalues are corresponding to the variances along the two new axis, their ratio, ranging from 0 to 1, gives a measure of the anisotropy of the sample. Hence, keeping in mind that HD collagen fibers have a parallel arrangement, while K shows randomly connected fibers, we expect a lower AR on HD, corresponding to a higher anisotropy, and a higher AR value in K.
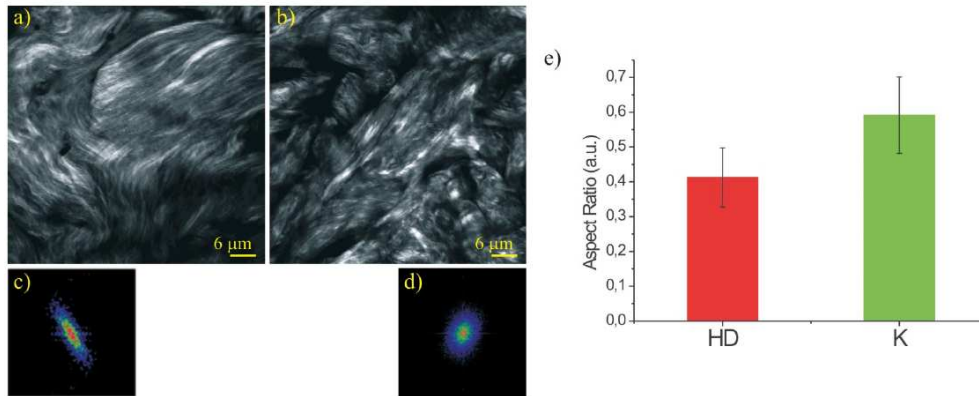
Figure 5.5: SHG transversal optical section of HD (a) and K (b). Corresponding 2D-DFT plot for HD (c) and K (d). Image analysis performed using ImageJ. Bar histogram of aspect ratio of FFT images for HD (red) and K (green). Data shown are calculated after averaging over all the examined sample.

The FFT plot of HD shows an elliptical profile (Fig.5.5c) as expected, while it is almost circular in K (Fig.5.5d). The histogram of the obtained values of AR is shown in Fig.5.5d. The value obtained for HD was 0.41 ± 0.08 and for K was 0.59 ± 0.09 . In order to take into account the biological variability

we took as error the standard deviation of data instead of the standard error. After a two sample statistical *t-test* the two calculated values were found to be statistically different at the 0.05 level. In conclusion, while using GLCM analysis we found an estimation of the organization within collagen fibers, with FFT analysis we can have a measurement on the mutual organization of fibers on a larger scale.

5.4 Conclusion

The aim of this work was to test different image pattern analysis methods on SHG images of skin tissue with dermal disorders. In particular we examined *ex vivo* samples of HD, NS and K. Every sample was imaged by combining TPEF with SHG microscopy. The obtained results were published on an international peer-reviewed journal [96].

As a first scoring method we used the SAAID index, with which we were able to characterize the tissue on a large scale (hundreds of μm) by means of elastin/collagen content. We had to average this index over a wide area in order to take into account its fluctuation and get physiological information. Further analysis on SHG images of HD and K were accomplished by GLCM image pattern analysis and statistical analysis on the Fourier domain. The resulting information coming out from the two methods are complementary. GLCM method is suitable to highlight intra-fiber bundle organization (less than 10 μm scale). Besides FFT provides informations on the mutual organization of collagen fibers (some hundreds of μm scale).

By relating the correlation length of the GLCM to fiber bundles diameter, we found thicker bundles in K than in HD, as expected. With FFT analysis we focused mainly on the organization of fibers and on their anisotropy. We found that a parallel arrangement of fibers, typical of HD, gives an elliptical profile in the Fourier domain, while random organization of collagen fibers in K yields to a circular distribution. Therefore using FFT we were able to find a score for collagen organization inside connective tissue.

In conclusion, each of the method presented is a promising analysis/scoring tool for classifying connective tissue at different scale. Furthermore their

5.4 Conclusion

combination is a powerful method to characterize connective tissues from a scale of hundreds of μm (SAAID) to less than 10 μm (GLCM). Therefore it is a potentially suitable tool for investigating collagen organization and remodeling after pharmacological or laser treatments on pathological scars.

CHAPTER 5. SCORING OF COLLAGEN ORGANIZATION IN HUMAN DERMIS BY TWO-PHOTON MICROSCOPY

Chapter 6

Conclusion and outlook

6.1   Conclusion

In this thesis I performed optical multi-dimensional analysis using a custom-built two-photon microscope equipped with a single-photon counting board forfluorescence lifetime imaging microscopy (FLIM) and multi-spectral two-photon excitation fluorescence (MTPE) measurements. The two-photon microscope was described and characterized in chapter 3. Radial and axial spatial resolutions achieved were 300 nm and 1400 nm, respectively. The FLIM set-up was also characterized and calibrated finding an instrumental response function (IRF) of 300 ps FWHM. By using the custom-built two-photon microscope it is possible to perform measurements which are laying on a multi-dimensional space. We emphasized its capability on both spectroscopic and morphological features.

In the former case we highlighted the spectroscopic capability of the two-photon microscope in performing time- and spectral- resolved imaging of fresh bladder biopsies (healthy bladder mucosa and carcinoma *in situ*). A lower second-harmonic generated (SHG) signal contribution from connective tissue of carcinoma *in situ* was evidenced by using SHG-to-autofluorescence ageing index of dermis (SAAID), defined as the ratio $SHG - TPE/TPE + SHG$. Besides in healthy mucosa, a higher value was found, indicating contributions from both collagen and cellular proliferation. A spectroscopic score was in-

troduced by using the "Red-Ox ratio", with which the balance/unbalance
of nicotinamide adenine dinucleotide (NADH)/flavin adenine dinucleotide
(FAD) content is highlighted. In carcinoma *in situ* (CIS) a higher fluo-
rescence contribution coming from NADH, in comparison with FAD, is at-
tributable to a predominance of glycolysis with respect to oxydative phos-
phorylation, typical of tumoral cells. Further information on cell metabolism
arose from FLIM analysis. By fitting the fluorescence exponential decay with
a double-exponential decay function $F(t) = a_1 exp(-t/\tau_1) + a_2 exp(-t/tau2)$,
with $\tau_1 < \tau_2$ it is possible to calculate the amplitude, a_1 and a_2, of the
"slow" and "fast" decay components, respectively. In carcinoma *in situ* a
distribution of a_1/a_2 centered around lower values indicates higher concen-
tration of protein-bound NADH. In healthy mucosa a higher concentration
of protein-bound FAD, with respect to CIS, could be related to the dom-
ination of phosphorylation as biochemical pathway for ATP production in
healthy cells. Further improvements of our multi-dimensional method arose
from morphological analysis. By measuring the cellular to nuclear dimension
ratio we found a higher ratio in HM with respect to CIS, as expected. In fact
tumoral cells usually shows a larger nuclear dimension.

In the second work on collagen pattern analysis of healthy dermis (HD),
normal scar (NS) and keloids (K), we emphasized the morphological capa-
bility of the two-photon microscope. The methods proposed are meant to
be complentary. In fact each method is well-suited to be used on different
spatial scales. We found that SAAID index is a powerful tool for tissue char-
acterization, able to evaluate the elastin/collagen content on a large scale
(hundreds of μm). Using SAAID score we highlighted an almost total ab-
sence of elastin in K while NS exhibited a higher elastin contribution. We
found grey-level co-occurrence matrix (GLCM) analysis well-suited for inves-
tigation on a smaller scale (below 10 μm). We calculated GLCM matrices
versus the neighbor index and we evaluated three different parameters as
correlation, homogeneity and energy. Correlation gives a score of the proba-
bility that a pixel and its neighbors have similar intensities. By fitting with
an exponential decay function the correlation versus the neighbor index it is
possible to calculate its typical decay length, also called correlation length.

6.1 Conclusion

It was possible to relate the correlation length to the collagen fiber thickness. The correlation length found for HD and K were 3.7 ± 0.1 μm and 6.8 ± 0.1 μm, respectively. HD showed a lower value in comparison to K, indicating thinner fiber as expected. Uniformity of K is evidenced by its higher values of energy and homogeneity with respect to HD. On an intermediate scale, Fast Fourier Transform (FFT) analysis was used for investigating collagen fibers organization. By looking at the profile of the FFT image it was possible to relate a parallel fiber arrangement to an elliptical FFT profile, while a total absence of organization will be reflected on a circular distribution. Therefore, the determination of the aspect ratio of the FFT plot distribution allowed us to have a score for tissue organization. As a result we found a higher organization in HD with respect to K.

In order to perform *in vivo* optical multi-dimensional analysis I designed and realized a multi-dimensional fiber-probe. The probe sacrifices the morphological information in order to have a fast acquisition and a short tissue exposure, required for *in vivo* analysis. Moreover the fiber-probe was designed with an outer diameter of 2.1 mm allowing its use in the service channel of a cystoscope. With the fiber-probe it is possible to investigate a small volume of tissue performing both fluorescence spectroscopy and lifetime measurements. Excitation can be accomplished at 378 nm and 445 nm, in order to excite NADH and FAD, respectively. The importance of the balance of these two molecules and their fluorescent lifetimes as "fingerprint" for cellular metabolism was emphasized in our work on bladder. A first test measurement of fluorescence spectroscopy was performed on a known fluorophore and on human skin. Fluorescence lifetime calibration was performed by using a fluorescent standard: Coumarin6. We measured a lifetime value of 2.5 ± 0.5 ns, in agreement with the value found in literature. Due to its flexibility and fast acquisition time the fiber-probe is a promising tool for *in vivo* optical multi-dimensional analysis of biological tissues.

Appendix A

Gray-Level Co-occurrence Matrix Analysis

Grey-Level Co-occurrence Matrix (GLCM) analysis is based on the calculation of score-indices of the GLCM matrix versus neighbor index [93, 94]. Given a starting image, the GLCM matrix at a certain neighbor index is calculated as follows: a new matrix is generated with a dimension N x N, where N is the bit-depth of the original image, and it is initialized to 0. Then, running pixel by pixel on the image, for each row (horizontal GLCM) we compare the pixel intensity value with the one of the neighbor pixel on the left (horizontal left GLCM) placed at a distance corresponding to the neighbor index. We report the pixel pair values on the GLCM matrix by increasing of one unit the corresponding cell in the matrix having the same coordinates of the pixel pair values. In order to understand the procedure, let's consider the image in Fig.A.1. In this case we have a grey-scale image of 4 bit-depth. Running the pixel index from [0,0] (upper left) and using a neighbor index of 1, the two first pixels values compared are (0,0), therefore on the corresponding 4 x 4 GLCM matrix we increase of one unit the value in the cell [0,0]. Iterating the routine for all the rows, the procedure gives as result the GLCM matrix shown in Fig.A.1.c. In the GLCM matrix is represented the number of recurrencies that a different combinations of pixel intensity values occurs. Referring to Fig.A.1.c, a value of 3 in the [2,2] position corresponds

to the number of times the combination (2,2) occurs in the original image. In order to take into account also co-occurence (from the right to the left) we sum the obtained matrix with its transposed. We evaluate also the vertical GLCM matrix in a similar way.

The final GLCM matrix is the normalized sum of the two, horizontal and vertical, matrices. On the GLCM diagonal it is represented the number of times that the neighbor pairs of pixels show the same value. Running the neighbor index from 1 up to n (n < N) we obtain n GLCM matrices with N x N dimensions.
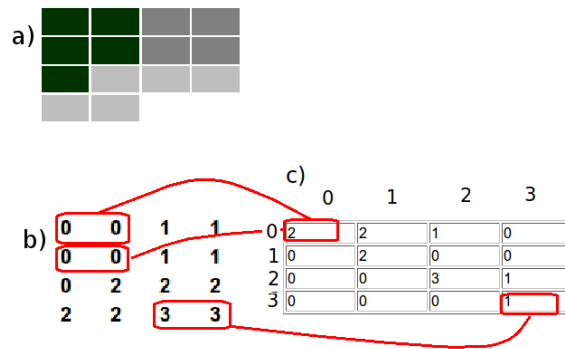
Figure A.1: Example of a 4 bit-depth grey scale image (a) and its corresponding numeric intensity values (b). The calculated GLCM matrix with neighbor index 1 (c).

There are three classes of parameters to be used for GLCM analysis: statistics, contrast and orderliness. In our analysis we considered one parameter per class.

Correlation R (statistics): it is a measure of the correlation of a pixel to its neighbor, calculated over the whole image as follows:

$$R = \sum_{i,j} \frac{(i - \mu_i)(j - \mu_j)p_{i,j}}{\sigma_i \sigma_j} \tag{A.1}$$

where $p_{i,j}$ are GLCM matrix elements, μ_i and μ_j the mean values of the i row and j column, σ_i and σ_j the standard deviations.

Homogeneity (Contrast): it gives a score of the probability that a pixel and its neighbors have similar intensities. It is calculated as follows:

$$H = \sum_{i,j} p_{i,j} \frac{1}{1 + (i+j)^2} \tag{A.2}$$

Energy (Orderliness): it provides a score of the uniformity of the image by using $p_{i,j}$ as a weight for itself, and it is calculated as follows:

$$E = \sqrt{\sum_{i,j} p_{i,j}^2} \tag{A.3}$$

APPENDIX A. GRAY-LEVEL CO-OCCURRENCE MATRIX ANALYSIS

Bibliography

[1] http://www.tutornext.com/stratified-specialized-epithelia/8614.

[2] R. Hoffman and L. Gross. Modulation contrast microscope. *Applied Optics*, 14(5):1169–1176, 1975.

[3] A. H. Coons, E. H. Leduc, M. H. Kaplan, and J. M. Connolly. Localization of antigen in tissue cells. *The Journal of Experimental Medicine*, 93(2):173–188, 1951.

[4] M. Chalfie, Y. Tu, G. Euskirchen, W. W. Ward, and D. C. Prasher. Green fluorescent protein as a marker for gene expression. *Science*, 263(5148):802–805, 1994.

[5] G. J. Brakenhoff. Imaging modes in confocal scanning light microscopy (cslm). *Journal of Microscroscopy*, 117:223, 1979.

[6] C. J. R. Sheppard and T. Wilson. Image formation in confocal scanning microscopes. *Optik*, 55:331, 1980.

[7] W. Denk, J.H. Strickler, and W.W. Webb. Two-photon laser scanning fluorescence microscopy. *Science*, 248(4951):73–76, 1990.

[8] M. Göppert-Mayer. Über elementarakte mit zwei quantensprüngen. *Annalen der Physik*, 401:273–294, 1931.

[9] W.R. Zipfel, R.M. Williams, and W.W. Webb. Nonlinear magic: multiphoton microscopy in the biosciences. *Nature Biotechnology*, 21:1369–1377, 2003.

[10] K. Konig. Multiphoton microscopy in life sciences. *Journal of Microscopy*, 200:83–104(22), November 2000.

[11] M. Rubart, E. Wang, K. W. Dunn, and L. J. Field. Two-photon molecular excitation imaging of ca2+ transients in langendorff-perfused mouse hearts. *American Journal of Physiology - Cell Physiology*, 284(6):C1654–1668, 2003.

[12] A. Volkmer, V. Subramaniam, D. J. Birch, and T. M. Jovin. One- and two-photon excited fluorescence lifetimes and anisotropy decays of green fluorescent proteins. *Biophysical Journal*, 78:1589–1598, 2000.

[13] S. Huang, H. Ahmed A., and W. W. Webb. Two-photon fluorescence spectroscopy and microscopy of nad(p)h and flavoprotein. *Biophysical journal*, 82:2811–2825, 2002.

[14] C. Xu, W. Zipfel, J. B. Shear, R. M. Williams, and W. W. Webb. Multiphoton fluorescence excitation: new spectral windows for biological nonlinear microscopy. *Proceedings of the National Academy of Sciences of the United States of America*, 93(20):10763–10768, 1996.

[15] M. J. Levene, D. A. Dombeck, K. A. Kasischke, R. P. Molloy, and W. W. Webb. In vivo multiphoton microscopy of deep brain tissue. *Journal of Neurophysiology*, 91(4):1908–1912, 2004.

[16] K. Konig and I. Riemann. High-resolution multiphoton tomography of human skin with subcellular spatial resolution and picosecond time resolution. *Journal of Biomedical Optics*, 8(3):432–439, 2003.

[17] K. König. Clinical multiphoton tomography. *Journal of Biophotonics*, 1:13–23, 2008.

[18] E. Dimitrow, M. Ziemer, M.J. Koehler, K. König, P. Elsner, and M.Kaatz. Sensitivity and specificity of multiphoton laser tomography for in vivo and ex vivo diagnosis of malignant melanoma. *Journal of Investigative Dermatology*, 129:1752–1758, 2009.

BIBLIOGRAPHY

[19] S. P. Tai, M. C. Chan, T. H. Tsai, S. H. Guol, L. J. Chen, and C. K. Sun. Two-photon fluorescence microscope with a hollow-core photonic crystal fiber. *Optics Express*, 12(25):6122–6128, Dec 2004.

[20] D. Bird and M. Gu. Two-photon fluorescence endoscopy with a micro-optic scanning head. *Optics Letters*, 28(17):1552–1554, 2003.

[21] L. Thiberville, S. Moreno-Swirc, T. Vercauteren, E. Peltier, C. Cave, and G. Bourg Heckly. In Vivo Imaging of the Bronchial Wall Microstructure Using Fibered Confocal Fluorescence Microscopy. *American Journal of Respiratory and Critical Care Medicine*, 175(1):22–31, 2007.

[22] M. T. Myaing, D. J. MacDonald, and X. Li. Fiber-optic scanning two-photon fluorescence endoscope. *Optics Letters*, 31(8):1076–1078, Apr 2006.

[23] P. J. Campagnola, M. Wei, A. Lewis, and L. M. Loew. High-resolution nonlinear optical imaging of live cells by second harmonic generation. *Biophysical Journal*, 77(6):3341–3349, 1999.

[24] T. Pons, L. Moreaux, O. Mongin, M. Blanchard-Desce, and J. Mertz. Mechanisms of membrane potential sensing with second-harmonic generation microscopy. *Journal of Biomedical Optics*, 8(3):428–431, 2003.

[25] D. A. Dombeck, K. A. Kasischke, H. D. Vishwasrao, M. Ingelsson, B. T. Hyman, and W. W. Webb. Uniform polarity microtubule assemblies imaged in native brain tissue by second-harmonic generation microscopy. *Proceedings of the National Academy of Sciences of the United States of America*, 100(12):7081–7086, 2003.

[26] P. J. Campagnola, A. C. M., M. Terasaki, P. E. Hoppe, C. J. Malone, and W. A. Mohler. Three-dimensional high-resolution second-harmonic generation imaging of endogenous structural proteins in biological tissues. *Biophysical Journal*, 82(1):493–508, 2002.

[27] M. Strupler, A. M. Pena, M. Hernest, P. L. Tharaux, J. L. Martin, E. Beaurepaire, and M. C. Schanne-Klein. Second harmonic imaging

and scoring of collagen in fibrotic tissues. *Optics Express*, 15(7):4054–4065, Apr 2007.

[28] T. Yasui, Y. Tohno, and T. Araki. Characterization of collagen orientation in human dermis by two-dimensional second-harmonic-generation polarimetry. *Journal of Biomedical Optics*, 9(2):259–264, 2004.

[29] P. Stoller, K. M. Reiser, P. M. Celliers, and A. M. Rubenchik. Polarization-modulated second harmonic generation in collagen. *Biophysical Journal*, 82(6):3330–3342, 2002.

[30] V. Da Costa, R. Wei, R. Lim, C. H. Sun, J. J. Brown, and B. J. F. Wong. Nondestructive imaging of live human keloid and facial tissue using multiphoton microscopy. *Archives of Facial Plastic Surgery*, 10(1):38–43, Jan/Feb 2008.

[31] M. Han, G. Giese, and J. Bille. Second harmonic generation imaging of collagen fibrils in cornea and sclera. *Optics Express*, 13(15):5791–5797, 2005.

[32] P. Matteini, F. Ratto, F. Rossi, R. Cicchi, C. Stringari, D. Kapsokalyvas, F. S. Pavone, and R. Pini. Photothermally-induced disordered patterns of corneal collagen revealed by shg imaging. *Optics Express*, 17(6):4868–4878, Mar 2009.

[33] Y. Guo, H. E. Savage, F. Liu, S. P. Schantz, P. P. Ho, and R. R. Alfano. Subsurface tumor progression investigated by noninvasive optical second harmonic tomography. *Proceedings of the National Academy of Sciences of the United States of America*, 96(19):10854–10856, 1999.

[34] S. Y. Breusegem, M. Levi, and N. P. Barry. Fluorescence correlation spectroscopy and fluorescence lifetime imaging microscopynephron experimental nephrology. *Nephron Exp. Nephron Experimental Nephrology*, 103:e41–e49, 2006.

[35] Y. Chen and A. Periasamy. Characterization of two-photon excitation fluorescence lifetime imaging microscopy for protein localization-

microscopy research and techniqu. *Microscopy Research and Technique*, 63:72–80, 2004.

[36] F. G. Cremazy, E. M. Manders, P. I. Bastiaens, G. Kramer, G. L. Hager, E. B. V. Munster, P. J. Verschure, T. J. Jr. Gadella, and R. Van Driel. Imaging in situ protein-dna interactions in the cell nucleus using fret-flim. *Experimental Cell Research*, 309:390–396, 2005.

[37] R. R. Duncan, A. Bergmann, M. A. Cousins, D. K. Apps, and M. J. Shipston. Multi-dimensional time-correlated single photon counting (tc-spc) fluorescence lifetime imaging microscopy (flim) to detect fret in cells. *Journal of Microscopy*, 215:1–12, 2004.

[38] J. Paoli, M. Smedh, A. Wennberg, and M. B. Ericson. Multiphoton laser scanning microscopy on non-melanoma skin cancer: Morphologic features for future non-invasive diagnostics. *Journal of Investigative Dermatology*, 128(optional):1248–1255, 2007.

[39] O. Warburg. The metabolism of tumor. *Constabel, London*, 1930.

[40] N. Ramanujam, R. Richards-Kortum, S. Thomsen, A. Mahadevan-Jansen, M. Follen, and B. Chance. Low temperature fluorescence imaging of freeze-trapped human cervical tissues. *Optics Express*, 8(6):335–343, 2001.

[41] W. Kaiser and C. G. B. Garrett. Two-photon excitation in caf_2: eu^{2+}. *Phys. Rev. Lett.*, 7(6):229–231, Sep 1961.

[42] L. Moreaux, O. Sandre, and J. Mertz. Membrane imaging by second-harmonic generation microscopy. *Journal of the Optical Society of America B*, 17(10):1685–1694, 2000.

[43] R. M. Williams, W. R. Zipfel, and W. W. Webb. Interpreting second-harmonic generation images of collagen i fibrils. *Biophysical Journal*, 88(2):1377–1386, 2005.

[44] W. R. Zipfel, R. M. Williams, R. Christie, A. Y. Nikitin, B. T. Hyman, and W. W. Webb. Live tissue intrinsic emission microscopy using multiphoton-excited native fluorescence and second harmonic generation. *Proceedings of the National Academy of Sciences of the United States of America*, 100(12):7075–7080, 2003.

[45] H. D. Vishwasrao, A. A. Heikal, K. A. Kasischke, and W. W. Webb. Conformational Dependence of Intracellular NADH on Metabolic State Revealed by Associated Fluorescence Anisotropy. *Journal of Biological Chemistry*, 280(26):25119–25126, 2005.

[46] M. C. Skala, K. M. Riching, A. Gendron-Fitzpatrick, J. Eickhoff, K. W. Eliceiri, J. G. White, and N. Ramanujam. In vivo multiphoton microscopy of NADH and FAD redox states, fluorescence lifetimes, and cellular morphology in precancerous epithelia. *Proceedings of the National Academy of Sciences*, 104(49):19494–19499, 2007.

[47] E. Gaviola. Ein fluorometer. apparat zur messung von fluoreszenzabklingungszeiten. *Zeitschrift für Physik A Hadrons and Nuclei*, 42:853–861, 1927. 10.1007/BF01776683.

[48] G. A. Elove, A. F. Chaffotte, H. Roder, and M. E. Goldberg. Early steps in cytochrome c folding probed by time-resolved circular dichroism and fluorescence spectroscopy. *Biochemistry*, 31(30):6876–6883, 1992.

[49] E. P. Diamandis. Immunoassays with time-resolved fluorescence spectroscopy: Principles and applications. *Clinical Biochemistry*, 21(3):139–150, 1988.

[50] R. Sanders, A. Draaijer, H. C. Gerritsen, P. M. Houpt, and Y. K. Levine. Quantitative ph imaging in cells using confocal fluorescence lifetime imaging microscopy. *Analytical Biochemistry*, 227(2):302–308, 1995.

[51] T. French, P. T. C. So, Jr D. J. Weaver, E. Gratton, Jr E. W. Voss, and J. Carrero. Two-photon fluorescence lifetime imaging microscopy

of macrophage-mediated antigen processing. *Journal of Microscopy*, 185:339–353, 1997.

[52] E. Gratton, S. Breusegem, J. Sutin, Q. Ruan, and N. Barry. Fluorescence lifetime imaging for the two-photon microscope: time-domain and frequency-domain methods. *Journal of Biomedical Optics*, 8(3):381–390, 2003.

[53] F. Duschinsky. Der zeitliche intensitätsverlauf von intermittierend angeregter resonanzstrahlung. *Zeitschrift für Physik A Hadrons and Nuclei*, 81:7–22, 1933. 10.1007/BF01341847.

[54] R. D. Spencer and G. Weber. Measurement of subnanosecond fluorescence lifetimes with a cross-correlation phase fluorometer. *Annals of the New York Academy of Sciences*, 169:361–376, 1969.

[55] G. Weber. Resolution of the fluorescence lifetimes in a heterogeneous system by phase and modulation measurements. *The Journal of Physical Chemistry*, 85(8):949–953, 1981.

[56] R.A. Colyer, C. Lee, and E. Gratton. A novel fluorescence lifetime imaging system that optimizes photon efficiency. *Microscopy Research and Technique*, 71:201–213, 2008.

[57] A. Meining, D. Saur, M. Bajbouj, V. Becker, E. Peltier, H. Höfler, C. H. von Weyhern, R. M. Schmid, and C. Prinz. In vivo histopathology for detection of gastrointestinal neoplasia with a portable, confocal miniprobe: An examiner blinded analysis. *Clinical Gastroenterology and Hepatology*, 5(11):1261–1267, 2007.

[58] N. D. Magee, J. S. Villaumie, E. T. Marple, M. Ennis, J. S. Elborn, and J. J. McGarvey. Ex vivo diagnosis of lung cancer using a raman miniprobe. *The Journal of Physical Chemistry B*, 113(23):8137–8141, 2009. PMID: 19453143.

[59] Z. Kirkali, T. Chan, M. Manoharan, F. Algaba, C. Busch, L. Cheng, L. Kiemeney, M. Kriegmair, R. Montironi, Wi. M. Murphy, I. A. Ses-

terhenn, M. Tachibana, and J. Weider. Bladder cancer: Epidemiology, staging and grading, and diagnosis. *Urology*, 66(6, Supplement 1):4–34, 2005. International Consultation on Bladder Tumors.

[60] M.l J. Droller. Biological considerations in the assessment of urothelial cancer: A retrospective. *Urology*, 66(5, Supplement 1):66–75, 2005.

[61] D. Jocham, F. Witjes, S. Wagner, B. Zeylemaker, J. van Moorslaar, M-O. Grimm, R. Muschter, G. Popken, F. Koenig, R. Knuechel, and K-H. Kurth. Improved detection and treatment of bladder cancer using hexaminolevulinate imaging: A prospective, phase iii multicenter study. *The Journal of Urology*, 174(3):862–866, 2005.

[62] P. Jichlinski and D. Jacqmin. Photodynamic diagnosis in non-muscle-invasive bladder cancer. *European Urology Supplements*, 7(7):529–535, 2008.

[63] P. Jichlinski, L. Guillou, S. J. Karlsen, P. U. Malmstroem, D. Jocham, B. Brennhovd, E. Johansson, T. Gaertner, N. Lange, H. van den Bergh, and H. J. Leisinger. Hexyl aminolevulinate fluorescence cystoscopy: A new diagnostic tool for photodiagnosis of superficial bladder cancer–a multicenter study. *The Journal of Urology*, 170(1):226–229, 2003.

[64] J. Schmidbauer, F. Witjes, N. Schmeller, R. Donat, M. Susani, and M. Marberger. Improved detection of urothelial carcinoma in situ with hexaminolevulinate fluorescence cystoscopy. *The Journal of Urology*, 171(1):135–138, 2004.

[65] J.C. Kennedy, R.H. Pottier, and D.C. Pross. Photodynamic therapy with endogenous protoporphyrin: Ix: Basic principles and present clinical experience. *Journal of Photochemistry and Photobiology B: Biology*, 6(1-2):143–148, 1990.

[66] S. Denzinger, M. Burger, B. Walter, R. Knuechel, W. Roessler, W. F. Wieland, and T. Filbeck. Clinically relevant reduction in risk of recurrence of superficial bladder cancer using 5-aminolevulinic acid-induced

fluorescence diagnosis: 8-year results of prospective randomized study. *Urology*, 69(4):675–679, 2007.

[67] D. I. Daniltchencko, C. R. Riedl, M. D. Sachs, F. Koenig, K. L. Daha, H. Pflueger, S. A. Loening, and D. Schnorr. Long-term benefit of 5-aminolevulinic acid fluorescence assisted transurethral resection of superficial bladder cancer: 5-year results of a prospective randomized study. *The Journal of Urology*, 174(6):2129–2133, 2005.

[68] Y. Fradet, H. B. Grossman, L. Gomella, S. Lerner, M. Cookson, D. Albala, and M. J. Droller. A comparison of hexaminolevulinate fluorescence cystoscopy and white light cystoscopy for the detection of carcinoma in situ in patients with bladder cancer: A phase iii, multicenter study. *The Journal of Urology*, 178(1):68–73, 2007.

[69] H. B. Grossman, L. Gomella, Y.Fradet, A. Morales, J. Presti, C. Ritenour, U. Nseyo, and M. J. Droller. A phase iii, multicenter comparison of hexaminolevulinate fluorescence cystoscopy and white light cystoscopy for the detection of superficial papillary lesions in patients with bladder cancer. *The Journal of Urology*, 178(1):62–67, 2007.

[70] B. Lovisa, P. Jichlinski, B. C. Weber, D. Aymon, H.t van den Bergh, and G. Wagnieres. High-magnification vascular imaging to reject false-positive sites in situ during hexvix[sup [registered sign]] fluorescence cystoscopy. *Journal of Biomedical Optics*, 15(5):051606, 2010.

[71] K. Steenkeste, S. Lecart, A. Deniset, P. Pernot, P. Eschwege, S. Ferlicot, S. Leveque-Fort, R. Briandet, and M. P. Fontaine-Aupart. Ex vivo fluorescence imaging of normal and malignant urothelial cells to enhance early diagnosis. *Photochemistry and Photobiology*, 83:1157–1166, 2007.

[72] S. M. Zhuo, J. X. Chen, T. Luo, X. S. Jiang, and S. S. Xie. Multiphoton microscopy of unstained bladder mucosa based on two-photon excited autofluorescence and second harmonic generation. *Laser Physics Letters*, 6:80–83, 2009.

[73] R. Yadav, S. Mukherjee, M. Hermen, G. Tan, F. R. Maxfield, W. W. Webb, and A. K. Tewari. Multiphoton microscopy of prostate and periprostatic neural tissue: A promising imaging technique for improving nerve-sparing prostatectomy. *Journal of Endourology*, 23(5):861–867, 2009. PMID: 19425823.

[74] L. H. Laiho, S. Pelet, T. M. Hancewicz, P. D. Kaplan, and P. T. C. So. Two-photon 3-d mapping of ex vivo human skin endogenous fluorescence species based on fluorescence emission spectra. *Journal of Biomedical Optics*, 10(2):024016, 2005.

[75] S. J. Lin, R. Jr. Wu, H. Y. Tan, W. Lo, W. C. Lin, T. H. Young, C. J. Hsu, J. S. Chen, S. H. Jee, and C. Y. Dong. Evaluating cutaneous photoaging by use of multiphoton fluorescence and second-harmonic generation microscopy. *Optics Letters*, 30(17):2275–2277, 2005.

[76] S. Alexander, G. Koehl, M. Hirschberg, E. Geissler, and P. Friedl. Dynamic imaging of cancer growth and invasion: a modified skin-fold chamber model. *Histochemistry and Cell Biology*, 130:1147–1154, 2008.

[77] R. Cicchi, A. Crisci, A. Cosci, G. Nesi, D. Kapsokalyvas, S. Giancane, M. Carini, and F. S. Pavone. Time- and spectral-resolved two-photon imaging of healthy bladder mucosa and carcinoma in situ. *Optics Express*, 18(4):3840–3849, 2010.

[78] A. Zoumi, A. Yeh, and B. J. Tromberg. Imaging cells and extracellular matrix in vivo by using second-harmonic generation and two-photon excited fluorescence. *Proceedings of the National Academy of Sciences of the United States of America*, 99(17):11014–11019, 2002.

[79] P. So, H. Kim, and I. Kochevar. Two-photon deep tissue ex vivo imaging of mouse dermal and subcutaneous structures. *Optics Express*, 3(9):339–350, 1998.

[80] B. R. Masters, P.T.C. So, and E. Gratton. Optical biopsy of in vivo human skin: Multi-photon excitation microscopy. *Lasers in Medical Science*, 13:196–203, 1998.

BIBLIOGRAPHY

[81] B. Masters and P. So. Confocal microscopy and multi-photon excitation microscopy of human skin in vivo. *Optics Express*, 8(1):2–10, 2001.

[82] J. C. Malone, A. F. Hood, T. Conley, J. Nurberg, L. A. Baldridge, J. L. Clendenon, and K. W. Dunn. Three-dimensional imaging of human skin and mucosa by two-photon laser scanning microscopy. *Journal of Cutaneous Pathology*, 29:453–458, 2002.

[83] Y. Sun, W. L. Chen, S. J. Lin, S. H. Jee, Y. F. Chen, L. C. Lin, P. T.C. So, and C. Y. Dong. Investigating mechanisms of collagen thermal denaturation by high resolution second-harmonic generation imaging. *Biophysical Journal*, 91(7):2620–2625, 2006.

[84] S. Roth and I. Freund. Second harmonic generation in collagen. *The Journal of Chemical Physics*, 70(4):1637–1643, 1979.

[85] M. J. Koehler, S. Hahn, A. Preller, P. Elsner, M. Ziemer, A. Bauer, K. Konig, R. Buckle, J. W. Fluhr, and M. Kaatz. Morphological skin ageing criteria by multiphoton laser scanning tomography: non-invasive in vivo scoring of the dermal fibre network. *Experimental Dermatology*, 17:519–523, 2008.

[86] S. J. Lin, S. H. Jee, C. J. Kuo, R. Jr. Wu, W. C. Lin, J. S. Chen, Y. H. Liao, C. J. Hsu, T. F. Tsai, Y. F. Chen, and C. Y. Dong. Discrimination of basal cell carcinoma from normal dermal stroma by quantitative multiphoton imaging. *Optics Letters*, 31(18):2756–2758, Sep 2006.

[87] P. Provenzano, K. Eliceiri, J. Campbell, D. Inman, J. White, and P. Keely. Collagen reorganization at the tumor-stromal interface facilitates local invasion. *BMC Medicine*, 4(1):38, 2006.

[88] R. Cicchi, D. Massi, S. Sestini, P. Carli, V. De Giorgi, T. Lotti, and F. S. Pavone. Multidimensional non-linear laser imaging of basal cell carcinoma. *Optics Express*, 15(16):10135–10148, Aug 2007.

[89] E Dimitrow, I. Riemann, A. Ehlers, M. J. Koehler, J. Norgauer, P. Elsner, K. König, and M. Kaatz. Spectral fluorescence lifetime detec-

tion and selective melanin imaging by multiphoton laser tomography for melanoma diagnosis. *Experimental Dermatology*, 18:509–515,, 2009.

[90] http://home.earthlink.net/ dayvdanls/IHP2.html.

[91] T. P. Amadeu, A. S. Braune, L. C. Porto, A. Desmoulière, and A. M. A. Costa. Fibrillin-1 and elastin are differentially expressed in hypertrophic scars and keloids. *Wound Repair and Regeneration*, 12:169–174, 2004.

[92] L. J. M. Meyer, S. B. Russell, J. D. Russell, J.S. Trupin, B. M. Egbert, S. Shuster, and R. Stern. Reduced hyaluronan in keloid tissue and cultured keloid fibroblasts. *The Journal of Investigative Dermatology*, 114:955–959, 2000.

[93] M. Hall-Beyer. The glcm tutorial homepage,. http://www.fp.ucalgary.ca/mhallbey/tutorial.htm, 2007.

[94] R. M. Haralick, K. Shanmugam, and I. Dinstein. Textural features for image classification. *IEEE Transactions on Systems, Man and Cybernetics*, 3:610–621, 1973.

[95] M.C. Branchet, S. Boisnic, C. Frances, C. Lesty, and L. Robert. Morphometric analysis of dermal collagen fibers in normal human skin as a function of age. *Archives of Gerontology and Geriatrics*, 13(1):1–14, 1991.

[96] R. Cicchi, D. Kapsokalyvas, V. De Giorgi, V. Maio, A. Van Wiechen, D. Massi, Torello Lotti, , and F. S. Pavone. Scoring of collagen organization in healthy and diseased human dermis by multiphoton microscopy. *Journal of Biophotonics*, 3:34–43, 2009.